Proprioceptive Coupling within Motor Neurons Drives C. Elegans Forward Locomotion

Proprioceptive coupling within motor neurons drives *C. elegans* forward locomotion

Quan Wen[1], Michelle Po[2], Elizabeth Hulme[3], Sway Chen[1], Xinyu Liu[3], Sen Wai Kwok[3], Marc Gershow[1], Andrew M Leifer[1], Victoria Butler[4,5], Christopher Fang-Yen[1,6], Taizo Kawano[2], William R Schafer[4], George Whitesides[3], Matthieu Wyart[7,*], Dmitri B Chklovskii[4,*], Mei Zhen[2,*], Aravinthan D T Samuel[1,*]

[1]Department of Physics and Center for Brain Science, Harvard University, Cambridge, MA, 02138

[2]Samuel Lunenfeld Research Institute, Mount Sinai Hospital, Toronto, ON M5G 1X5, Canada

[3]Department of Chemistry, Harvard University, Cambridge, MA, 02138

[4]MRC Laboratory of Molecular Biology, University of Cambridge, Cambridge, UK

[5]Janelia Farm Research Campus, HHMI, Ashburn, VA, 20147

[6]Department of Bioengineering, University of Pennsylvania, Philadelphia, PA, 19104

[7]Department of Physics, New York University, New York, NY, 10003

[*]Corresponding author

Running title: Proprioceptive coupling drives *C. elegans* locomotion

Summary

Locomotion requires coordinated motor activity throughout an animal's body. In both vertebrates and invertebrates, chains of coupled Central Pattern Generators (CPGs) are commonly evoked to explain local rhythmic behaviors. In *C. elegans*, we report that proprioception within the motor circuit is responsible for propagating and coordinating rhythmic undulatory waves from head to tail during forward movement. Proprioceptive coupling between adjacent body regions transduces rhythmic movement initiated near the head into bending waves driven along the body by a chain of reflexes. Using optogenetics and calcium imaging to manipulate and monitor motor circuit activity of moving *C. elegans* held in microfluidic devices, we found that the B-type cholinergic motor neurons transduce the proprioceptive signal. In *C. elegans*, a sensorimotor feedback loop operating within a specific type of motor neuron both drives and organizes body movement.

Introduction

All locomotory circuits, from invertebrates to limbed vertebrates, must generate rhythmic activities throughout their motor systems (Delcomyn, 1980; Grillner, 2003; Marder and Calabrese, 1996). To exhibit coherent gaits like crawling, walking, swimming, or running, the rhythmic activities of all body parts must be patterned in specific temporal sequences (Delcomyn, 1980; Grillner, 2003; Marder and Calabrese, 1996; Mullins et al., 2011). Rhythmic motor activities are typically generated by dedicated neural circuits with intrinsic rhythmic activities called the Central Pattern Generators (CPG) (Brown, 1911; Delcomyn, 1980; Grillner, 2003; Kiehn, 2011; Marder and Calabrese, 1996; Mullins et al., 2011). Networks of CPGs can be distributed throughout a locomotory circuit. For example, chains of CPGs have been identified along the nerve cord of the leech and distributed CPG modules have also been found in mammalian lumbar spinal cord to control hindlimb movement (Kiehn, 2006). In isolated nerve cords or spinal cords, even after all muscle and organ tissues have been removed, motor circuits that correspond to different body parts generate spontaneous rhythmic activity, a fictive resemblance of the swimming patterns in behaving animals (Cohen and Wallen, 1980; Kristan

and Calabrese, 1976; Mullins et al., 2011; Pearce and Friesen, 1984; Wallen and Williams, 1984).

When a chain of CPGs generates autonomous rhythmic activities, where each CPG corresponds to a different body part, mechanisms to coordinate their activities must be present. Sensory feedback often plays a critical role in this coordination (Grillner and Wallen, 2002; Mullins et al., 2011; Pearson, 1995, 2004). In lamprey and leech, for example, specialized proprioceptive neurons in the spinal cord and body wall modulate the spontaneous activity of CPGs within each body segment (Cang and Friesen, 2000; Cang et al., 2001; Grillner et al., 1984). Activation of these stretch-sensitive neurons, either by current injection or by externally imposed body movements, can entrain CPG activity (McClellan and Jang, 1993; Yu and Friesen, 2004). Similarly, in limbed vertebrates, sensory feedback from mechanoreceptors in the skin and muscle, working through interneuronal circuits that modulate the rhythmic bursting of motor neurons, helps to coordinate limb movements during step cycles (Pearson, 2004).

Here, we study undulatory wave propagation along the body of the nematode *Caenorhabditis elegans* during forward movement (Figure 1A). The worm offers an opportunity to obtain a complete systems-level understanding of a locomotory circuit. The adult motor circuit has been mapped at synaptic resolution (Chen et al., 2006; White et al., 1986). Recent advances in optical neurophysiology (Chronis et al., 2007; Clark et al., 2007; Faumont et al., 2011; Kawano et al., 2011; Leifer et al., 2011; Liewald et al., 2008; Zhang et al., 2007) now make it possible to explore the physiology of this motor circuit in freely moving animals.

C. elegans locomotion is controlled by a network of excitatory cholinergic (A and B types) and inhibitory GABAergic (D-type) motor neurons along the nerve cord that innervate the muscle cells lining the worm body (White et al., 1976). Earlier cell ablation studies suggest that B-type cholinergic motor neurons are specifically required for forward locomotion (Chalfie et al., 1985). The 7 VB and 11 DB neurons innervate the ventral and dorsal musculature, respectively (Figure 1). The A-type cholinergic motor neurons, necessary for backward movement (Chalfie et al., 1985), are similarly divided into the D and V subclasses that innervate the dorsal and ventral musculature (not shown in Figure 1).

How the *C. elegans* motor circuit organizes bending waves along its body during locomotion is poorly understood. Even when all premotor interneurons are ablated (Kawano et al., 2011; Zheng et al., 1999), *C. elegans* retains the ability to generate local body bending, suggesting that the motor circuit itself (A, B, and D-type neurons and muscle cells) can generate undulatory waves. However, the synaptic connectivity of the motor circuit does not contain motifs that might be easily interpreted as local CPG elements that could spontaneously generate oscillatory activity, e.g., oscillators driven by mutual inhibition between two neuronal classes that can be found in larger animals (Figure 1B). The synaptic connectivity does contain a pattern to avoid simultaneous contraction of both ventral and dorsal muscles; the VB and DB motor neurons that activate the ventral and dorsal muscles also activate the opposing inhibitory GABAergic motor neurons (DD and VD, respectively). However, this contralateral inhibition generated by GABAergic neurons is not essential for rhythmic activity along the body or the propagation of undulatory waves during forward locomotion (McIntire et al., 1993).

In addition, unlike larger animals, the *C. elegans* motor circuit does not contain specialized proprioceptive or mechanosensory afferents that are positioned to provide information about local movements to each body region through local sensory or interneurons (Fig. 1b). The DVA interneuron has been shown to have proprioceptive properties (Hu et al., 2011; Li et al., 2006), but its process spans the whole worm body and is not required for forward locomotion. The lack of specialized sensory neurons within the motor circuit led Russell and Byerly to speculate that individual motor neurons might themselves have proprioceptive properties (White et al., 1986). In particular, electron microscopy showed that the cholinergic motor neurons have long undifferentiated processes that extend along the nerve cord without making synapses (Fig. 1c) (White et al., 1986). A putative mechanosensory channel UNC-8 is also expressed in motor neurons (Tavernarakis et al., 1997). However, whether any motor neuron is capable of proprioception, or how proprioception is used by the motor circuit, has not been demonstrated.

Biomechanical evidence also implies a role for proprioception in *C. elegans* locomotion as its gait adapts to the mechanical load imposed by the environment (Berri et al., 2009; Fang-Yen et al., 2010). When worms swim in low load environments like water, the bending wave has a long

wavelength (~ 1.5 body length *L*). When crawling or swimming in high load environments ~10,000-fold more viscous than water, the bending wave has a short wavelength (~ 0.65 *L*). But whether or how proprioception might be related to gait adaptation has not been determined.

Here, we examined whether the worm motor circuit has proprioceptive properties and how these properties are connected to undulatory dynamics. We apply novel microfluidic devices and *in vivo* optical neurophysiology to show that proprioceptive coupling between adjacent body segments constitutes the trigger that drives bending wave propagation from head to tail. We found that posterior body regions are compelled to bend in the same direction and shortly after the bending of the neighboring anterior region. We localize this new form of proprioceptive coupling to the B-type cholinergic motor neurons. We quantify the spatial and temporal dynamics of this proprioceptive coupling, and use our biophysical measurements to calculate its role on undulatory dynamics. Proprioception in the *C. elegans* motor circuit, beyond simply explaining the propagation of an undulatory wave from head to tail, also provides a quantitative explanation for gait adaptation to external load.

Results

The bending of one body region requires the bending of its anterior neighbor

C. elegans moves forward by propagating dorsal-ventral body bending waves from head to tail. The detailed kinematics of bending waves can be quantified by measuring curvature at each point along the body centerline over time (Figure 2A). To measure κ, we first calculate R, the radius of curvature at each point along the centerline ($\kappa = 1/R$). To compare data from different animals, we measure distance along the worm body as the fractional distance from head to tail (head = 0; tail = 1), and normalize curvature using L, the total length of the body centerline (normalized curvature = $\kappa \times L$). Thus, during sustained forward movement, each body region alternates between positive and negative curvature, and bands of curvature propagate from head to tail as shown in a kymogram (red: positive; blue: negative) (Figure 2B,C). Curvatures measured near the head tend to be larger than curvatures measured near the tail (Fig. 2D)

First, we asked how the motor activity in one body region might be affected by the bending of neighboring body regions. To do this, we designed microfluidic devices that immobilized body regions of varying length (Figure 3A,B and Movie S1). Our first device trapped the center of a worm in a narrow straight channel to keep it from bending without impeding worm movement either anterior or posterior to the channel (Figure 3A,B). We used a channel diameter (40 μm) that was sufficient to immobilize the trapped region of a young adult worm (worm diameter is 54 ± 4 μm; mean ± SD) with minimum constriction.

We consistently recorded bouts of forward movement (> 10 s) when we immobilized a middle portion of the worm (Fig. 3A-C). Bending waves would propagate normally to the anterior limit of the channel (green data points in Figure 3D). Short channels (100 μm long) did not affect wave propagation to the tail; the bending wave that emerged from the posterior limit of the channel (black data points in Figure 3D) exhibited similar amplitude as a free swimming worm (Figure 2D). However, increasing channel length beyond 200 μm significantly diminished the bending amplitude in the posterior body region (Figure 3D). Increasing channel length also augmented the bending amplitude of the anterior body region, perhaps reflecting an increased

effort to escape the channel. Fixing the channel length, but moving it towards the tail also reduced the posterior bending amplitude (Figure 3E).

To determine how immobilization affects muscle activity within and posterior to the channel, we quantified intracellular calcium dynamics in the muscle cells of transgenic animals co-expressing the calcium indicator GCaMP3 (25) and RFP in all body wall muscles (Figure S1 and Movie S2). In these animals, intracellular calcium levels can be inferred from the ratio of green to red fluorescence. Whereas muscle cells anterior to the channel exhibited strong rhythmic calcium dynamics during the propagation of bending waves, muscle cells within and posterior to the channel did not (Figure S1). Thus, immobilizing a body region disrupts the propagation of bending waves by lowering motor circuit activity within and posterior to that region. The tail was held rigid and straight in the absence of muscle activity because of the high internal hydrostatic pressure of worms.

Taken together, these results suggest that immobilizing a portion of the worm can directly override rhythmic activity. Motor activity in a posterior region requires the active bending of an anterior region extending ~ 200 μm.

Muscle activity is positively correlated with the curvature of adjacent anterior neighbors

To further explore how the bending of adjacent body regions is coupled, we designed microfluidic devices that trapped the middle region of a worm at defined curvatures (Figure 4A,C). We used channels that were at least 250 μm long to prevent bending waves from propagating into the unrestrained posterior part. We found that the unrestrained posterior region exhibited fixed curvature in the same direction as that imposed on the middle trapped region (e.g., compare the overall shape of the posterior region to the trapped region in Figure 4A and the measured curvature of the posterior region to the trapped region in the kymogram in Figure 4B; also see Movie S3). By using channels with different curvatures, we found that the curvature of the posterior region increased linearly with the imposed curvature on the trapped middle region with slope 0.62 ± 0.03 L (Figure 4C; Figure S2A,B).

We verified that the fixed curvature of the unrestrained posterior region was due to a fixed pattern of muscle activity. First, by using a transgenic strain that expresses halorhodopsin (Han and Boyden, 2007) in all body wall muscles (P*myo-3*::*NpHR*), we were able to induce muscle relaxation in the posterior region with green light illumination. The tail reversibly straightened during illumination (Figure 4D-F and Movie S4). Second, we directly monitored muscle activity in the curved posterior region using the muscle calcium reporter GCaMP3 (Figure 4G). In the posterior region emerging from the channel, we consistently measured higher calcium levels in the muscle cells on the inner side than the outer side of the curved body (Figure 4H,I and Movie S5). Third, when the whole animal was paralyzed with sodium azide, the body regions emerging from the curved channel remained straight, instead of following the curvature imposed by the channel (Movie S6).

These results suggest that the bending of anterior body regions dictates the bending of posterior body regions during forward movement. Posterior regions bend in the same direction, and in proportion to, the bend of anterior regions.

Post-channel body curvature follows channel curvature with a viscosity-dependent delay

Next, we measured the time lag between the bending in one body region and the induced bending in the posterior region. To do this, we designed pneumatic microfluidic devices to rapidly change the curvature of a trapped worm (Figure 5A). We flanked both sides of the immobilizing channel with independently controllable inflatable chambers. As with static channels, we found that the curvature of the posterior body was positively correlated with channel curvature. Switching channel curvature towards the dorsal or ventral side induced a corresponding switch in the curvature of the posterior body (Figure 5B-C and Movie S7). This result underscores dorsal/ventral symmetry in the mechanism that couples the curvature of adjacent body regions.

We found that the switch in curvature of the posterior region propagated with measurable speed from the channel to the tail, consistent with the flow of a retrograde bending signal (Figure 5D-F). To assess whether the delayed bending of the posterior region represented mechanical

damping by the external viscous fluid or internal delays within the neuromuscular network, we studied worms in fluids of different viscosity (Figure 5D-F). We found that the bending delay was roughly constant, ~300 ms, in fluids ranging from 1 mPa·s (the viscosity of water) to ~100 mPa·s. In more viscous fluids, the bending delay began to increase, becoming ~ 1 s at 300 mPa·s. These results suggest that ~300 ms represents an upper bound for delays within the neuromuscular network, which are rate-limiting at low viscosities. These neuromuscular delays might reflect delays in synaptic transmission and/or the limiting speed of muscle contraction.

Local proprioceptive coupling is transduced by B-type motor neurons

The *C. elegans* wiring diagram offers a small number of candidate cell-types within the motor circuit that might play roles in generating or propagating a local proprioceptive signal: the A-type cholinergic motor neurons, B-type cholinergic motor neurons, the D-type GABAergic motor neurons, and muscle cells. One neuron outside the motor circuit, the DVA interneuron, has also been shown to exhibit proprioceptive properties. We sought to determine which cell-type was responsible for coupling the bending activities of adjacent body regions through proprioception.

First, we trapped transgenic worms that expressed halorhodopsin in all cholinergic motor neurons (P*unc-17*::*NpHR*) in the pneumatic devices, and illuminated them with green light. We found that light-induced hyperpolarization of the cholinergic neurons prevented the posterior body regions from following induced changes in the curvature of the anterior region (Figure 6A-C and Movie S8). Instead, optogenetic inactivation of the cholinergic neurons locked the posterior region in the posture as it was immediately preceding illumination.

Second, we studied *vab*-7 mutants, which have specific defects in the morphology of the dorsal B-type cholinergic motor neurons. In these mutants, the DB neurons reverse the orientation of their axons so that they project anteriorly instead of posteriorly(Esmaeili et al., 2002) (Figure S3A) The *vab-7* mutation does not affect the ventral B-type motor neurons. During unrestrained forward movement, the bending wave near the head of *vab-7* mutants was normal. However, the bending wave that propagates to posterior regions was biased toward the ventral side (Figure

S3B, D). When we trapped *vab-7* mutants in the pneumatic channels, the posterior region was only able to follow channel bending to the ventral side, not to the dorsal side (Figure S3C, F-G). These results suggest that the dorsal and ventral B-type cholinergic motor neurons are each responsible for propagating dorsal and ventral curvatures to posterior body regions.

Third, we compared the effects of specifically inactivating the A-, B-, and D-type motor neurons. To do this, we examined transgenic animals in which either the A- or B-type cholinergic motor neurons are specifically deactivated by an active K+ channel (P*unc-4*::*twk-18*(gf)-*UrSL-wCherry* and P*acr-5*::*twk-18*(gf)-*UrSL-wCherry*, respectively) (Kawano et al., 2011; Kunkel et al., 2000), as well as *unc-25* mutants that lack the GABA neurotransmitter required by the D-type motor neurons (Jin et al., 1999). During forward locomotion, the bending waves of animals propagated from head to tail when either the A- or D-type motor neurons were inactivated (Figure S4A, C). When trapping the worm in the pneumatic microfluidic device, the posterior region of these worms followed the induced body bending towards either side (Figure S4B, D). In contrast, inactivating the B-type motor neurons prevented an induced bend from anterior regions from propagating to posterior regions (Figure 6D-F and movie S9). When the B-type motor neurons were inactivated, the curvature of the posterior region was not locked to the curvature of the trapped region (Figure 6E) as for wild type worms (Figure 4B).

The *C. elegans* motor circuit does not possess local sensory or interneurons that convey local bending information to B-type motor neurons. The DVA interneuron, whose axon spans the whole worm body and connects with most DB motor neurons, has been shown to have proprioceptive properties (Hu et al., 2011; Li et al., 2006). We thus asked whether DVA plays a role in propagating local bending information during forward locomotion. However, we found that laser killing DVA does not disrupt the ability of the posterior region to follow the curvature of the anterior region (Figure S4G-H). Taken together, these results show that neither the A-type, D-type motor neurons, nor the DVA interneuron are needed to propagate the bending signal from anterior to posterior regions. However, the B-type motor neurons are essential.

Gap junctions between muscle cells do not contribute to proprioceptive coupling

We also asked whether the body muscle cells themselves might propagate bending signals from anterior to posterior regions. Adjacent body wall muscle cells are connected by gap junctions mediated specifically by an innexin UNC-9, providing a possible, alternative pathway for transducing the proprioceptive signal (Figure 1B) (Liu et al., 2006). First, we trapped transgenic worms expressing halorhodopsin in their muscle cells (P*myo-3::NpHR*) in the pneumatic channel. We found that specifically relaxing the muscles in the trapped curved region with green light illumination had no effect on the curvature of the free posterior region (Figure S4E-F). We also tested transgenic animals that lacked these gap junctions in their muscle cells. To do this, we used a transgenic *unc-9* mutant animal in which *unc-9* expression was restored in UNC-9 expressing cells except the body wall muscles. We found that these transgenic animals were fully capable of propagating an imposed bend from anterior to posterior regions (Figure S4H).

As a further test of gap junctions between muscle cells, we optogenetically stimulated body segments in transgenic worms expressing Channelrhodopsin-2 in body wall muscles (P*myo*-3::*ChR*2) without input from motor neurons. To abolish motor neuron inputs, we treated transgenic worms with ivermectin, which hyperpolarizes the motor circuit by activating glutamate gated chloride channel (Cully et al., 1994), but is not known to affect body wall muscles (Hart (ed.)). Optogenetically inducing ventral or dorsal bending in targeted body segments of paralyzed animals did not induce bending of neighboring regions ($n > 10$ and Figure S5A-B and Movie S10). We observed similar phenomenon when ivermectin treatment was performed in the *unc-13(s69)* ($n > 10$), a loss of function mutation that eliminates synaptic input from motor neurons to muscles (Richmond et al., 1999). These experiments suggest that gap junctions between muscles are insufficient to propagate bending signals between neighboring body regions.

Interestingly, when we optogenetically induced body bending in ivermectin-treated paralyzed worms, the bend would persist long after turning off the illumination (Figure S5A-B and Movie S10). The bend would gradually relax over ~ 40 s, but often in a series of abrupt jumps (Figure S5C). This observation suggests that body wall muscles can exhibit hysteresis: maintaining

stable levels of contraction long after stimulation. This observation could also explain why inactivating cholinergic motor neurons in transgenic worms (P*unc-17*::*NpHR*) locks them in the posture immediately preceding illumination [Figure 6A-C and (Leifer et al., 2011)].

Bending directly activates B-type motor neurons

Our results thus suggest that the B-type cholinergic motor neurons represent the locus for proprioceptive coupling along the motor circuit. Next, we sought direct physiological evidence for the proprioceptive properties of the B-type motor neurons. First, we measured the intracellular calcium dynamics of individual DB and VB neurons of unrestrained worms swimming inside microfluidic chambers (*Pacr-5-GCaMP3-UrSL-wCherry*). Consistent with an earlier study (Kawano et al., 2011), the calcium dynamics of DB6 and VB9, two motor neurons that innervate the opposing dorsal and ventral body wall muscles respectively, are negatively correlated with one another during forward movement (Figure 7A). The cross-correlation between the time-varying calcium signals from DB6 and VB9 are presented in Figure 7B1. Furthermore, we measured the cross-correlation between motor neuron activity and the local curvature of the worm at the position of the motor neurons. We found that the activity of the ventral motor neuron is positively correlated with bending towards the ventral side (Figure 7B2), and the activity of the dorsal cholinergic neuron is positively correlated with bending towards the dorsal side (Figure 7B3). These results confirm that the sign and amount of local bending is strongly coupled to the sign and amount of activity in the B-type motor neurons.

To determine whether the bending of anterior regions directly determines the activity of posterior B-type motor neurons, we visualized their calcium dynamics using our curved microfluidic channels. When we imposed a curvature on the middle portion of a worm, bending waves propagated normally from the head to the anterior limit of the channel. When we positioned specific DB and VB motor neurons near the anterior limit of the channel, we observed rhythmic activity correlated with dorsal and ventral bending, respectively (Figure 7C1). When we positioned the same DB and VB motor neurons within or near the posterior limit of the channel, we observed fixed patterns of activity that reflected the curvature imposed by the channel. Bending the worm towards the dorsal side activated the DB motor neuron over the VB motor

neuron (Figure 7C2 and Figure 7D). Bending the worm towards the ventral side activated the VB motor neuron over the DB motor neuron (Figure 7C3 and Figure 7D). These fixed patterns of B-type motor neuron activities relaxed when the worm spontaneously transitioned to backward movement (Figure 7C2, 7C3).

Proprioception is consistent with gait adaptation in response to mechanical load

Unlike larger well-studied swimmers like the leech and lamprey, *C. elegans* is smaller than the capillary length of water (~ 2 mm). At this size, forces due to surface tension that hold the crawling animal to substrates are 10,000-fold larger than forces due to the viscosity of water(Sauvage, 2007). Thus, the motor circuit of *C. elegans* must adapt to extreme ranges of external load. When worms swim in low load environments like water, the bending wave has a long wavelength (~ 1.5 body length L). When crawling or swimming in high load environments ~10,000-fold more viscous than water, the bending wave has a short wavelength (~ 0.65 L). We asked whether the spatiotemporal dynamics of proprioceptive coupling between body regions might play a role in this gait adaptation.

In our model, we assert that the undulatory wave begins with rhythmic dorsal/ventral bends near the head of a worm. Along the body, however, we assert only the dynamics of proprioceptive coupling measured here and previously measured biomechanics of the worm body. We model the muscles in each body region as being directly activated by bending detected in the neighboring anterior region. We can infer the spatial extent of this coupling l to be ~ 200 μm based on our direct measurements (Figure 3D). For a one millimeter-long worm freely swimming in water, the maximum speed of undulatory wave propagation from head to tail is ~ 2.6 mm/s. Thus, we can estimate the limiting delay τ_c for transducing a bending signal from region to region to be ~ 80 ms. The simplest linear model for motor circuit activity along the body is fully defined in terms of these parameters, along with biomechanical parameters that were measured in previous work (Fang-Yen et al., 2010): the mechanical drag imposed by the environment and the bending modulus of the worm b. This model can be solved analytically for the wavelength of bending waves, λ:

$$\lambda = \frac{2\pi l}{\omega C_N (\lambda/2\pi)^4 / b + \omega \tau_c} \quad (1)$$

Here, $C_N \approx 30\eta$ is the frictional drag coefficient normal to the body centerline, where η is the fluid viscosity. $b = 9.5 \times 10^{-14}$ Nm^2 and ω is the angular frequency of undulation in fluid with different viscosities (Fang-Yen et al., 2010). Equation (1) predicts a specific dependence of bending wavelength on fluid viscosity that closely fits experimental observations (Figure 8 and Supplementary Information).

Proprioception within the motor circuit provides a simple explanation for the propagation of bending waves along the motor circuit. Each body region is compelled to bend shortly after the bending of anterior regions, so that the rhythmic bending activity initiated near the head can generate a wave of rhythmic activity that travels along the whole body. When viewed within the biomechanical framework of the worm body, the spatiotemporal dynamics of proprioception within the motor circuit provides a new explanation for the adaptation of undulatory gait on mechanical load.

Discussion

Prevailing models for rhythmic movements in larger animals involve networks of CPGs that are modulated and entrained by sensory feedback (Marder and Bucher, 2001). For example, the lamprey spinal cord consists of approximately 100 independent CPG units distributed along its length (Cangiano and Grillner, 2003), In most systems, coherent rhythmic movements across the whole body are organized by proprioceptive and mechanosensory feedback to CPG units (McClellan and Jang, 1993; Pearson, 1995; Yu and Friesen, 2004). In the leech, muscle activity between body segments can be coordinated by sensory feedback even after severing the neuronal connectivity between segments (Yu et al., 1999). In *Drosophila* larvae, specific classes of mechanosensory neurons are required to propagate peristaltic waves during locomotion (Cheng et al., 2010; Hughes and Thomas, 2007; Song et al., 2007).

In *C. elegans,* however, a distribution of CPGs along the motor circuit remains to be identified. In contrast, we found a previously undescribed role for proprioception within the motor circuit for propagating rhythmic activities along the body. We show that during forward locomotion, bending waves are driven along the body through a chain of reflexes connecting the activity of neighboring body segments. Unlike larger animals, *C. elegans* does not have dedicated local sensory or interneurons that might generate or propagate proprioceptive signals within the motor circuit. The cellular economy of the *C. elegans* wiring diagram implies that individual neurons may have high levels of complexity. Indeed, we have found that the proprioceptive feedback loop that drives forward locomotion is transduced within motor neurons themselves, specifically the B-type cholinergic neurons. The activity of each VB and DB motor neuron is directly activated by ventral and dorsal bending of an anterior region, respectively. Axons of adjacent B-type cholinergic neurons are not anatomically restricted to specific segments, but partially overlap with one another in the ventral and dorsal nerve cords. Thus, going from head to tail, a large posterior portion of each B-type cholinergic neuron runs parallel to the anterior portion of its neighbor in the ventral and dorsal nerve cords. These overlapping portions, along with gap junctions between adjacent neurons, provide a mechanism for propagating a bending signal from neuron to neuron (Figure S6).

We note that another aspect of the anatomy of the B-type motor neurons led Russell and Byerly to propose that these neurons might have proprioceptive properties. Both DB and VB motor neurons have long undifferentiated processes that extend posteriorly beyond their regions of synaptic output to the muscle cells (Figure 1C). If proprioception were specifically localized to these processes, they would communicate bending signals from posterior to anterior. Because the B-type neurons propagate signals from anterior to posterior, as we have found, the long posterior projections of the B-type motor neurons are unlikely to represent the specialized “proprioceptive antennae”.

One candidate for a potential mechanosensory channel expressed in the cholinergic motor neurons is the *unc-8* gene that encodes a putative mechanically gated ion channel. However, an *unc-8(lf)* mutation did not disrupt proprioceptive coupling between neighboring body regions

(Figure S4H). Thus, the molecular mechanism that confers proprioceptive properties to the B-type motor neurons remains to be identified.

We have shown that proprioception within the motor circuit can translate the rhythmic activity near the head into undulatory waves that travel along the body. This form of sensory feedback also makes the motor circuit directly responsive to the external environment. We used our biophysical measurements to calculate the effect of proprioception within the motor circuit on undulatory waves in surroundings with different viscosities, and uncovered a compelling explanation for the adaptation of undulatory wavelength on external load. At low loads, the worm undulates with a long wavelength. At high loads, the worm undulates with a short wavelength. This dependence has an intuitive biomechanical explanation. As external viscosity increases, it takes longer for a posterior body region to bend in response to any curvature change in its anterior neighbor. Increasing the time scale of the bending response increases the phase difference between the shapes of neighboring body segments, leading to a smaller undulation wavelength.

The small size and experimental accessibility of the *C. elegans* motor circuit allows the possibility of modeling locomotion that integrates the dynamics of all neuronal and muscular components. Our results suggest that a full model of *C. elegans* locomotion must integrate the biomechanics of undulatory movement with neuromuscular activity to properly incorporate the role of proprioception within the motor circuit.

Figure legends

Figure 1: A schematic diagram of the motor circuit in *C. elegans*.

(A) Worms undulate by alternating contraction and relaxation of dorsal and ventral muscle cells lining the body. Dorsal bending is achieved when dorsal muscle cells contract (filled cells) and ventral muscle cells relax (open cells). Ventral bending is achieved when ventral muscle cells contract and dorsal muscle cells relax.

(B) General patterns of connectivity in the wiring diagram for forward movement. Arrows indicate excitatory chemical synapses from the cholinergic motor neurons (VB and DB). Blunt ended lines indicate inhibitory chemical synapses from GABAergic motor neurons (DD and VD). GABAergic neurons are dispensable for the propagation of the bending wave along the worm body during forward movement. Dashed lines indicate gap junctions between neighboring muscle cells and neighboring neurons of each cell type. Six to twelve neurons of each cell type are distributed along the worm body. The schematic diagram is based on refs. (Chen, 2007; Durbin, 1987; White et al., 1986).

(C) The morphology of DB and VB motor neurons along the circuit. All cell bodies are located in the ventral nerve cord. The axons of VB motor neurons have short anterior axons and long posterior axons. The axons of the DB motor neurons cross to the dorsal nerve cord with long posterior projections.

Figure 2. Quantification of undulatory dynamics

(A) Worm undulatory dynamics is quantified using time-varying curvature along the body. Points along the centerline of length L can be specified in terms of fractional distance from the head (head = 0; tail = 1). The radius of curvature R can be measured at all points along the body. Curvature, κ, is the reciprocal of R. To represent bending in non-dimensional units, we calculate a normalized curvature as κ multiplied by worm length L.

(B) Video images of a worm swimming forward. A red-blue colormap illustrates alternating curvatures at fractional distance = 0.5.

(C) Kymogram of time-varying curvature illustrating retrograde bending waves along the worm represented in non-dimensional units.

(D) Bending magnitude along the body of a wild-type freely swimming worm, measured as the standard deviation of normalized curvature over time. n = 18 worms, mean ± one standard error.

Figure 3. Bending of posterior regions requires anterior bending

(A) Schematic of microfluidic device. *a* stands for anterior region, *p* stands for posterior region, and *t* stands for trapped region of a worm. PDMS: Polydimethylsiloxane.

(B) Video images of a wild-type young adult worm exhibiting forward undulatory gait inside the microfluidic device (also see Movie S1). The channel divides the worm body into unrestrained anterior, posterior, and trapped middle regions.

(C) Kymogram of time-varying curvature along the body of the worm shown in **(B)**. Gray lines mark the anterior and posterior limits of the straight channel.

(D) Bending magnitude of a posterior and an anterior body region (~ 0.15 worm length) adjacent to the channel, measured as the standard deviation of time-varying normalized curvature, is plotted as a function of the length of the trapped region. $n \geq 10$ worms for each condition, mean ± one standard error. Position of the posterior limit of the channel is 0.7 ± 0.1 (mean ± standard deviation) for each condition, measured as the fractional distance from head to tail. $*P<0.05$, $***P < 0.001$, Mann-Whitney U test.

(E) Bending magnitude of a posterior body region (mean ± one standard error) decreases with the position of the posterior limit of the channel (R = -0.24, $p < 0.05$, Spearman's rank correlation test). We measured 64 bouts of forward movement trapped in different channel positions from 20 worms. Channel length is 300 μm.

Figure 4. Bending of posterior regions is positively correlated with anterior bending.

(A) Video images of a worm exhibiting forward undulatory gait while partially constrained in a curved microfluidic channel (also see Movie S3).

(B) Kymogram of normalized curvature of the worm shown in **(A).** Gray lines show anterior and posterior limits of the curved channel.

(C) The curvature of the unrestrained posterior body region, measured as a spatial average from the posterior limit of the channel to the tail and a temporal average over bouts of forward movement, is plotted as a function of channel curvature. Each data point (mean ± one standard error) represents data from at least 8 animals. Magenta line is the linear least square fit.

(D) Video images of a transgenic worm (P*myo-3*::*NpHR*) partially constrained in a curved microfluidic channel. The green bar indicates a 2 s interval during which the posterior body wall muscles emerging from the channel was hyperpolarized by green light illumination (also see Movie S4).

(E) Kymogram of normalized curvature of the animal shown in **(D)**. Green shading indicates the body region and duration of green light illumination.

(F) Mean curvature ± one standard error of the posterior region emerging from the curved channels as shown in **(D)** during green light illumination (~ 30 measurements using 6 worms).

(G) Calcium imaging of body wall muscles in a partially constrained transgenic worm (P*myo-3*::*GCaMP3::RFP*) in a curved channel. Red fluorescence from RFP constitutes the reference signal. Green fluorescence from GCaMP3 indicates intracellular calcium levels. The contours of the microfluidic channel are drawn in white (also see Movie S5).

(H) Comparison of the ratio of green fluorescence to red fluorescence intensity emitted from inner and outer muscles of the posterior body region. Each data point represents a spatial average of the ratio over a posterior body region (~ 0.2 worm length) adjacent to the channel and a temporal average over a bout of forward movement. Solid lines indicate population mean. Among 14 measurements from 6 worms, six measurements restrict dorsal muscles on the inner side. ***$P < 0.001$, Wilcoxon signed rank test.

(I) Representative ratiometric kymogram of calcium levels in inner and outer muscle cells of a worm trapped in the device shown in **(G)**. Higher/lower ratios of green fluorescence to red fluorescence in each set of body wall muscles indicate higher/lower intracellular calcium levels. Arrows highlight one calcium wave that propagates from the head to the anterior limit of the curved channel along the inner musculature and outer musculature.

Figure 5. Pneumatic microfluidic device for manipulating body curvature.

(A) Schematic of the pneumatic microfluidic device. The channel is flanked by two chambers. Alternatively pressurizing one chamber while depressurizing the other rapidly switches the curvature the curvature of a region of a trapped worm.

(B) Video images of a partially immobilized wild-type worm. At $t = 0$ s, the channel starts to change its curvature (also see Movie S7).

(C) Two representative curvature kymograms of a worm trapped in the pneumatic channel. Gray lines mark the anterior and posterior limits of the curved channels. White dashed lines at $t = 0$ s mark the induced change in channel curvature from negative (color blue) to positive (color red). While the unrestricted anterior body region exhibits opposite bending activities in the two

kymograms, this difference did not affect the dynamics of the induced curvature change in the unrestricted posterior body region. The bending wave that shifts the posterior region from negative to positive curvature propagates with a velocity v that is the reciprocal slope of the zero crossing in curvature (color black). A white line is drawn along the zero crossing, and velocity is calculated from its angle with respect to the vertical axis, $v = \tan\theta$.

(D) The time course of curvature change in the immediate posterior region (~ 0.1 worm length) emerging from the pneumatic channel after the switch of channel curvature at $t = 0$ s. The two curves correspond to experiments conducted in two different viscosities. Error bars indicate one standard error.

(E) The time constant for relaxation of the posterior region to new curvatures obtained by fitting exponentials to time courses as shown in **(D).** Each data point represents at least 30 measurements from five worms. Error bars indicate 95% confidence interval to the exponential fits.

(F) The speed of the bending wave following induced changes in channel curvature as a function of fluid viscosity. Error bars indicate one standard error.

Figure 6. B-type cholinergic motor neurons are required for transducing the proprioceptive signal.

(A) Video images of a transgenic worm (P*unc-17::NpHR*) partially trapped in a pneumatic microfluidic channel. Green bar indicates the duration of green light illumination of the middle portion of the worm before and after induced change in channel curvature at $t = 0$ s. As a result, the curvature of the tail failed to follow the curvature change of the channel (also see Movie S8).

(B) Curvature kymogram of the transgenic worm trapped in the channel as shown in **(A)**. Green shading indicates the body region and duration of green light illumination.

(C) Curvature of the posterior body region, measured as an average from the posterior limit of the channel to the tail, during onset of illumination (green shading) and the induced change in curvature of the middle region at $t = 0$ (dashed line). Representative data from five worms were shown. Red curve corresponds to the experiment shown in **(A)** and **(B)**. A comparison with Figure 4D shows that posterior body region did not switch its curvature after induced curvature change in the trapped middle region during green light illumination.

(D) Video images of a P*acr*-5::*twk-18*(gf)-*UrSL-wCherry* transgenic worm partially trapped in a static microfluidic channel. B-type cholinergic motor neurons in this strain were specifically deactivated due to the expression of an active K^+ channel.

(E) Curvature kymogram of the partially trapped worm shown in **(D)** during periods of forward movement. A comparison with Figure 3b shows that the posterior body region emerged from the channel no longer follow the curvature of the middle region imposed by the channel.

(F) The mean curvature of the posterior body region emerged from the microfluidic channel in wild type (n = 8) and P*acr*-5::*twk*-18(gf)-*UrSL-wCherry* transgenic worms (n = 9) during forward movement. All worms were partially trapped in the channel with a curvature 6-8 mm^{-1}. *** $p < 0.001$, Mann-Whitney U test.

Figure 7. Calcium imaging of B-type motor neuron activity induced by bend-sensitive coupling

(A) Calcium imaging of B motor neuron activity in a forward moving worm. Worms can generate and propagate dorsal and ventral bending waves along the body without restriction. Upper panel: fluorescent video images of two adjacent motor neurons VB9 and DB6 in an unrestrained transgenic worm (P*acr-5*::*GCaMP3-UrSL-wCherry*) swimming within a microfluidic chamber. Middle panel: intracellular calcium dynamics of VB9 and DB6. Lower panel: curvature of the corresponding body region. The intracellular calcium activity can be inferred from the ratio of *GCaMP3* fluorescence intensity to *wCherry* fluorescence intensity. Red fluorescence from wCherry constitutes the reference signal. $\Delta R/R$ is the relative deviation of the emission ratio from the baseline.

(B1) Cross correlation between VB9 and DB6 calcium dynamics of forward moving worms. **(B2)** Cross correlation between VB9 calcium dynamics and the curvature of corresponding body region. **(B3)** Cross correlation between DB6 calcium dynamics and the curvature of corresponding body region. n = 9 and error bars indicate one standard error.

(C1) Representative intracellular calcium dynamics of motor neurons DB6 and VB9 located anterior to the channel. During forward movement, these two neurons exhibited anti-correlated oscillatory calcium activities. **(C2)** Intracellular calcium dynamics of VB9 and DB6 when the body region containing both neurons was imposed to bend towards the dorsal side. DB6

sustained a higher level of calcium activity. **(C3)** Calcium dynamics of VB9 and DB6 when the body region containing both neurons was imposed to bend towards the ventral side. VB9 sustained a higher level of calcium activity. In both cases, the calcium dynamics in VB9 and DB6 inactivated during reversal.

(D) Difference of intracellular calcium activity between DB6 and VB9 when the body region containing both neurons were imposed to bend either towards dorsal or ventral side. This quantity is normalized by the total calcium activity of DB6 and VB9 and averaged over a time period (> 20 s) when a worm was moving forward. Each black line represents a different worm and magenta triangles represent the population mean. ** $p < 0.005$, Wilcoxon signed rank test. $n = 10$ worms.

Figure 8. The dynamics of proprioception within the motor circuit are consistent with continuous gait adaptation

Theoretically predicted dependence of undulation wavelength on external viscosity [red, also see Equation (1)] closely fit the experimental measurements (blue). Error bars are 95% confidence interval.

Experimental procedures

Worm strains and cultivation

Wild-type, transgenic, and mutant worms were cultivated using standard methods (Brenner, 1974). Detailed strain information can be found in the Supplementary Information. The transgenic worms used in all optogenetic experiments were cultivated in the dark at 20^{o}C on NGM plates with *Escherichia coli* OP50 and all-*trans* retinal. We performed all experiments using young adult worms within a few hours after their final molt.

Microfluidic devices

Custom microfluidic devices were fabricated in PDMS using soft lithography techniques. In the pneumatic microfluidic device, the channel was flanked by two chambers that could be alternatively pressurized and depressurized with a valve system under computer control using custom software written in LabVIEW (National Instruments, Austin, TX). We loaded each microfluidic channel with NGM buffer or dextran solution [~20% dextran in NGM (wt/vol) in most cases]. An individual worm was flowed into the inlet of each microfluidic channel and worm position within each channel was manually controlled by syringes connected to polyethylene tubing.

Measuring undulatory dynamics

Experiments were performed on Nikon microscopes (TE2000 or Eclipse LV150) under 4X magnification with dark field illumination. Image sequences were taken by a CCD camera (Imaging Source) and recorded on a computer at 30 Hz using IC Capture software (Imaging Source). Image analysis was performed using custom software written in MATLAB (MathWorks, Inc. Natick, MA) following methods described in (Fang-Yen et al., 2010).

Calcium imaging of body wall muscle activities

We imaged calcium dynamics within muscle cells of worms partially trapped in microfluidic channels, using similar methods described in (Chen, 2007). GCaMP3 and RFP were excited by LEDs filtered at 448-492nm and 554-572nm respectively using Semrock single-bandpass filters. Fluorescence emission was recorded through an Olympus MVX Plan Apochromat 2X objective

(working distance 20mm, numerical aperture 0.5). The fluorescence image was split by a Cairns Optosplit II Image Splitter and the two images (green channel, 499-525 nm; red channel, 581-619 nm) were projected onto two halves of an Andor iXon 885 EMCCD camera. A DinoLite Pro AM413T USB camera was used to track the worm using Worm Tracker 2.0 software developed by the Schafer lab. Zaber T-LSR075A Motorized Linear Slides give automated x-y stage movement. Imaging sequences were recorded on a computer at 10 Hz using Andor Solis software and converted into TIFF files using ImageJ. Images were then analyzed using custom-written MATLAB scripts. Briefly, the two split images were re-aligned and the calcium activities of muscles were calculated as the ratio of green to red fluorescence emission intensities. The true emission intensities from the two channels are calculated using the following formulas: True green = green measured – green background; True red = red measured – red background – 0.153×True green. There is 15.3% bleedthrough from the green to the red channel.

Calcium Imaging of B-type motor neurons

We imaged calcium dynamics in B-type cholinergic motor neurons of worms moving in the microfluidic device using a spinning-disk confocal microscopy (Yokogawa). GCaMP3 and wCherry, which are co-expressed in the B-type motor neurons, were excited by a 488 nm blue laser and a 561 nm yellow laser (Andor Technology) alternatively at every 30 ms. Fluorescence emission was collected through a Nikon Plan Apo 20x objective (working distance 1 mm, numerical aperture 0.75) and projected onto an Andor iXon2 EMCCD camera. Imaging sequences were recorded using the NIS-elements software and converted into TIFF files. Images were then analyzed using custom-written MATLAB scripts. The motor neurons of interest were automatically identified and the calcium dynamics in the cells were calculated as the ratio of GCaMP3 to wCherry fluorescence emission intensities from two sequential images using the following formula:

$$R = \frac{I_b - \varepsilon_r I_y}{I_y - \varepsilon_g I_b} \frac{1+\varepsilon_g}{1+\varepsilon_r} \tag{2}$$

where I_b is total fluorescence emission intensity excited by the blue laser and I_y is the total fluorescence emission intensity excited by the yellow laser. ε_r is the ratio of mCherry emission intensity excited by the blue laser to that excited by the yellow laser. ε_g is the ratio of GCaMP3 emission intensity excited by the yellow laser to that excited by the blue laser. ε_r = 0.0356 and ε_g

≈ 0 when the same blue and yellow laser power was used. These ratios were measured using strains expressing only wCherry or GCaMP3 in given neurons.

To measure the correlation between intracellular calcium dynamics in the B-type motor neurons and the bending activity in the corresponding body region, we used canny edge detection method to identify the boundaries of the worm body from the fluorescence images and calculated the curvature of the body segment where the cell body of the motor neurons are located. The cross correlation between calcium activities and curvature was calculated using the following formula:

$$C_{xy}(\tau) = \frac{\langle \Delta x(t+\tau)\Delta y(t) \rangle}{\sqrt{\langle \Delta x^2(t) \rangle}\sqrt{\langle \Delta y^2(t) \rangle}} \quad (3)$$

where $\Delta x(t)$ and $\Delta y(t)$ are deviations of x and y from their respective means and $\langle \cdot \rangle$ denotes the average over time.

Optogenetic stimulation

We used two optical setups to stimulate transgenic worms expressing Channelrhodopsin or Halorhodopsin. Experiments with the pneumatic microfluidic device were conducted on a Nikon microscope (Eclipse LV150) under 10X magnification with dark field illumination. A mercury arc lamp with green filter and field diaphragm was used to illuminate the worm with controlled spot size. Rhodamine in the microfluidic channel (10 μM) allowed us to directly visualize the area and duration of green light illumination.

Other Optogenetic experiments were performed using a modified version of the CoLBeRT system, described in (Leifer et al., 2011). Briefly, the CoLBeRT system consists of an inverted Nikon microscope (TE2000), blue and green diode pumped solid state lasers, a high speed CCD camera, and a digital micromirror device all under the control of the open source MindControl software. Worm was imaged under red light with dark field illumination, and the digital micromirror device reflected laser light to shine on targeted cells or regions of the worm. For the *unc-13*; P*myo*-3::*ChR2* and ivermectin-treated worm experiments, the CoLBeRT system was modified to programmatically control laser intensity. To do this, the MindControl software interfaces with custom-written LabVIEW software that modulated the analog voltage signal sent

to the laser power controllers via a LabJack U3-HV. MindControl and associated software is available at http://github.com/samuellab.

References

Berri, S., Boyle, J.H., Tassieri, M., Hope, I.A., and Cohen, N. (2009). Forward locomotion of the nematode C. elegans is achieved through modulation of a single gait. HFSP Journal 3, 186-193.
Brenner, S. (1974). The genetics of Caenorhabditis elegans. Genetics 77, 71-94.
Brown, T.G. (1911). The Intrinsic Factors in the Act of Progression in the Mammal. P Roy Soc Lond B Bio 84, 308-319.
Cang, J., and Friesen, W.O. (2000). Sensory modification of leech swimming: rhythmic activity of ventral stretch receptors can change intersegmental phase relationships. Journal of Neuroscience 20, 7822-7829.
Cang, J., Yu, X., and Friesen, W.O. (2001). Sensory modification of leech swimming: interactions between ventral stretch receptors and swim-related neurons. J Comp Physiol A 187, 569-579.
Cangiano, L., and Grillner, S. (2003). Fast and slow locomotor burst generation in the hemispinal cord of the lamprey. Journal of neurophysiology 89, 2931-2942.
Chalfie, M., Sulston, J.E., White, J.G., Southgate, E., Thomson, J.N., and Brenner, S. (1985). The Neural Circuit for Touch Sensitivity in Caenorhabditis-Elegans. Journal of Neuroscience 5, 956-964.
Chen, B.L. (2007). Neuronal Network of C. elegans: from Anatomy to Behavior. In The Watson School of Biological Sciences (Cold Spring Harbor Cold Spring Harbor Laboratory), p. 96.
Chen, B.L., Hall, D.H., and Chklovskii, D.B. (2006). Wiring optimization can relate neuronal structure and function. P Natl Acad Sci USA 103, 4723-4728.
Cheng, L.E., Song, W., Looger, L.L., Jan, L.Y., and Jan, Y.N. (2010). The role of the TRP channel NompC in Drosophila larval and adult locomotion. Neuron 67, 373-380.
Chronis, N., Zimmer, M., and Bargmann, C.I. (2007). Microfluidics for in vivo imaging of neuronal and behavioral activity in Caenorhabditis elegans. Nat Methods 4, 727-731.
Clark, D.A., Gabel, C.V., Gabel, H., and Samuel, A.D.T. (2007). Temporal activity patterns in thermosensory neurons of freely moving Caenorhabditis elegans encode spatial thermal gradients. J Neurosci 27, 6083-6090.
Cohen, A.H., and Wallen, P. (1980). The neuronal correlate of locomotion in fish. "Fictive swimming" induced in an in vitro preparation of the lamprey spinal cord. Exp Brain Res 41, 11-18.
Cully, D.F., Vassilatis, D.K., Liu, K.K., Paress, P.S., Van der Ploeg, L.H., Schaeffer, J.M., and Arena, J.P. (1994). Cloning of an avermectin-sensitive glutamate-gated chloride channel from Caenorhabditis elegans. Nature 371, 707-711.
Delcomyn, F. (1980). Neural basis of rhythmic behavior in animals. Science 210, 492-498.
Durbin, R.M. (1987). Studies on the development and organisation of the nervous system of Caenorhabditis elegans. (University of Cambridge), p. 121.

Esmaeili, B., Ross, J.M., Neades, C., Miller, D.M., 3rd, and Ahringer, J. (2002). The C. elegans even-skipped homologue, vab-7, specifies DB motoneurone identity and axon trajectory. Development 129, 853-862.
Fang-Yen, C., Wyart, M., Xie, J., Kawai, R., Kodger, T., Chen, S., Wen, Q., and Samuel, A.D. (2010). Biomechanical analysis of gait adaptation in the nematode Caenorhabditis elegans. Proc Natl Acad Sci U S A 107, 20323-20328.
Faumont, S., Rondeau, G., Thiele, T.R., Lawton, K.J., McCormick, K.E., Sottile, M., Griesbeck, O., Heckscher, E.S., Roberts, W.M., Doe, C.Q., and Lockery, S.R. (2011). An image-free opto-mechanical system for creating virtual environments and imaging neuronal activity in freely moving Caenorhabditis elegans. PLoS One 6, e24666.
Grillner, S. (2003). The motor infrastructure: from ion channels to neuronal networks. Nat Rev Neurosci 4, 573-586.
Grillner, S., and Wallen, P. (2002). Cellular bases of a vertebrate locomotor system-steering, intersegmental and segmental co-ordination and sensory control. Brain Res Brain Res Rev 40, 92-106.
Grillner, S., Williams, T., and Lagerback, P.A. (1984). The edge cell, a possible intraspinal mechanoreceptor. Science 223, 500-503.
Han, X., and Boyden, E.S. (2007). Multiple-color optical activation, silencing, and desynchronization of neural activity, with single-spike temporal resolution. PLoS One 2, e299.
Hart (ed.), A.C. Behavior. In WormBook, T.C.e.R. Community, ed. (WormBook).
Hu, Z., Pym, E.C., Babu, K., Vashlishan Murray, A.B., and Kaplan, J.M. (2011). A neuropeptide-mediated stretch response links muscle contraction to changes in neurotransmitter release. Neuron 71, 92-102.
Hughes, C.L., and Thomas, J.B. (2007). A sensory feedback circuit coordinates muscle activity in Drosophila. Mol Cell Neurosci 35, 383-396.
Jin, Y., Jorgensen, E., Hartwieg, E., and Horvitz, H.R. (1999). The Caenorhabditis elegans gene unc-25 encodes glutamic acid decarboxylase and is required for synaptic transmission but not synaptic development. Journal of Neuroscience 19, 539-548.
Kawano, T., Po, M.D., Gao, S., Leung, G., Ryu, W.S., and Zhen, M. (2011). An Imbalancing Act: Gap Junctions Reduce the Backward Motor Circuit Activity to Bias C. elegans for Forward Locomotion. Neuron 72, 572-586.
Kiehn, O. (2006). Locomotor circuits in the mammalian spinal cord. Annu Rev Neurosci 29, 279-306.
Kiehn, O. (2011). Development and functional organization of spinal locomotor circuits. Curr Opin Neurobiol 21, 100-109.
Kristan, W.B., Jr., and Calabrese, R.L. (1976). Rhythmic swimming activity in neurones of the isolated nerve cord of the leech. J Exp Biol 65, 643-668.
Kunkel, M.T., Johnstone, D.B., Thomas, J.H., and Salkoff, L. (2000). Mutants of a temperature-sensitive two-P domain potassium channel. Journal of Neuroscience 20, 7517-7524.
Kuroyanagi, H., Kobayashi, T., Mitani, S., and Hagiwara, M. (2006). Transgenic alternative-splicing reporters reveal tissue-specific expression profiles and regulation mechanisms in vivo. Nat Methods 3, 909-915.
Leifer, A.M., Fang-Yen, C., Gershow, M., Alkema, M.J., and Samuel, A.D. (2011). Optogenetic manipulation of neural activity in freely moving Caenorhabditis elegans. Nat Methods 8, 147-152.

Li, W., Feng, Z., Sternberg, P.W., and Xu, X.Z. (2006). A C. elegans stretch receptor neuron revealed by a mechanosensitive TRP channel homologue. Nature 440, 684-687.
Liewald, J.F., Brauner, M., Stephens, G.J., Bouhours, M., Schultheis, C., Zhen, M., and Gottschalk, A. (2008). Optogenetic analysis of synaptic function. Nat Methods 5, 895-902.
Liu, Q., Chen, B., Gaier, E., Joshi, J., and Wang, Z.W. (2006). Low conductance gap junctions mediate specific electrical coupling in body-wall muscle cells of Caenorhabditis elegans. J Biol Chem 281, 7881-7889.
Marder, E., and Bucher, D. (2001). Central pattern generators and the control of rhythmic movements. Curr Biol 11, R986-996.
Marder, E., and Calabrese, R.L. (1996). Principles of rhythmic motor pattern generation. Physiol Rev 76, 687-717.
McClellan, A.D., and Jang, W. (1993). Mechanosensory inputs to the central pattern generators for locomotion in the lamprey spinal cord: resetting, entrainment, and computer modeling. J Neurophysiol 70, 2442-2454.
McIntire, S.L., Jorgensen, E., Kaplan, J., and Horvitz, H.R. (1993). The GABAergic nervous system of Caenorhabditis elegans. Nature 364, 337-341.
Mullins, O.J., Hackett, J.T., Buchanan, J.T., and Friesen, W.O. (2011). Neuronal control of swimming behavior: comparison of vertebrate and invertebrate model systems. Prog Neurobiol 93, 244-269.
Pearce, R.A., and Friesen, W.O. (1984). Intersegmental coordination of leech swimming: comparison of in situ and isolated nerve cord activity with body wall movement. Brain Res 299, 363-366.
Pearson, K.G. (1995). Proprioceptive regulation of locomotion. Curr Opin Neurobiol 5, 786-791.
Pearson, K.G. (2004). Generating the walking gait: role of sensory feedback. Prog Brain Res 143, 123-129.
Richmond, J.E., Davis, W.S., and Jorgensen, E.M. (1999). UNC-13 is required for synaptic vesicle fusion in C. elegans. Nat Neurosci 2, 959-964.
Sauvage, P. (2007). Etude de la locomotion chez C. elegans et perturbations mecaniques du mouvement. In Laboratoire Matiere et Systemes Compiexes (Paris, Universite Paris Diderot-Paris 7), p. 152.
Song, W., Onishi, M., Jan, L.Y., and Jan, Y.N. (2007). Peripheral multidendritic sensory neurons are necessary for rhythmic locomotion behavior in Drosophila larvae. Proc Natl Acad Sci U S A 104, 5199-5204.
Tavernarakis, N., Shreffler, W., Wang, S., and Driscoll, M. (1997). unc-8, a DEG/ENaC family member, encodes a subunit of a candidate mechanically gated channel that modulates C. elegans locomotion. Neuron 18, 107-119.
Wallen, P., and Williams, T.L. (1984). Fictive locomotion in the lamprey spinal cord in vitro compared with swimming in the intact and spinal animal. J Physiol 347, 225-239.
White, J.G., Southgate, E., Thomson, J.N., and Brenner, S. (1976). The structure of the ventral nerve cord of Caenorhabditis elegans. Philos Trans R Soc Lond B Biol Sci 275, 327-348.
White, J.G., Southgate, E., Thomson, J.N., and Brenner, S. (1986). The structure of the nervous system of the nematode Caenorhabditis elegans. Philos Trans R Soc Lond B Biol Sci 314, 1-340.
Yu, X., and Friesen, W.O. (2004). Entrainment of leech swimming activity by the ventral stretch receptor. J Comp Physiol A Neuroethol Sens Neural Behav Physiol 190, 939-949.
Yu, X.T., Nguyen, B., and Friesen, W.O. (1999). Sensory feedback can coordinate the swimming activity of the leech. J Neurosci 19, 4634-4643.

Zhang, F., Wang, L.P., Brauner, M., Liewald, J.F., Kay, K., Watzke, N., Wood, P.G., Bamberg, E., Nagel, G., Gottschalk, A., and Deisseroth, K. (2007). Multimodal fast optical interrogation of neural circuitry. Nature 446, 633-639.
Zheng, Y., Brockie, P.J., Mellem, J.E., Madsen, D.M., and Maricq, A.V. (1999). Neuronal control of locomotion in C. elegans is modified by a dominant mutation in the GLR-1 ionotropic glutamate receptor. Neuron 24, 347-361.

Figure 1

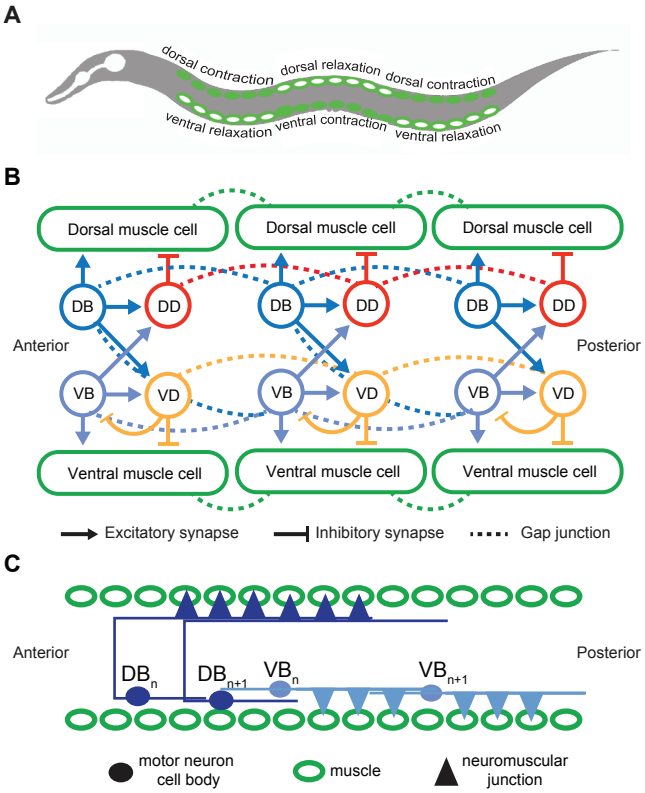
A
dorsal contraction
dorsal relaxation
dorsal contraction
ventral relaxation
ventral contraction
ventral relaxation
B
Dorsal muscle cell
Dorsal muscle cell
Dorsal muscle cell
DB
DD
DB
DD
DB
DD
Anterior
Posterior
VB
VD
VB
VD
VB
VD
Ventral muscle cell
Ventral muscle cell
Ventral muscle cell
Excitatory synapse
Inhibitory synapse
Gap junction
C
Anterior
Posterior
DBn
DBn+1
VBn
VBn+1
motor neuron cell body
muscle
neuromuscular junction

Figure 2

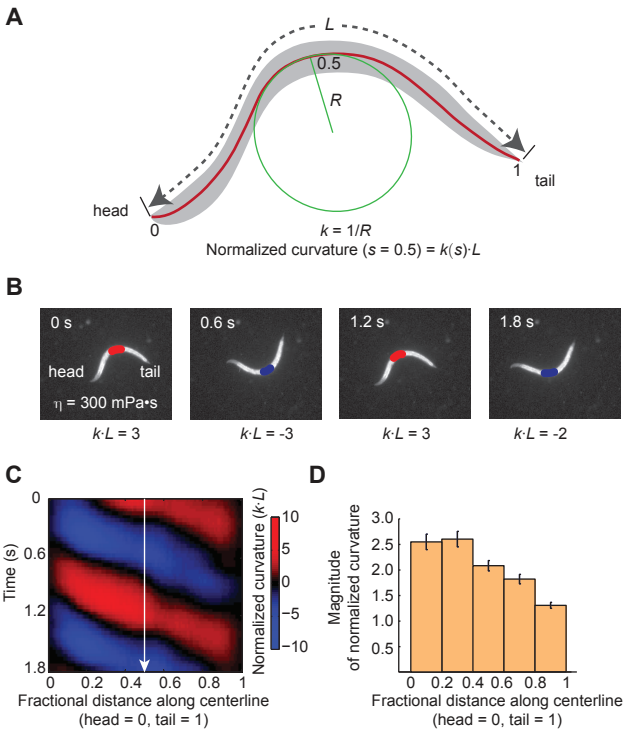
A
L
0.5
R
head
0
1
tail
k = 1/R
Normalized curvature (s = 0.5) = k(s)·L
B
0 s
head
tail
η = 300 mPa•s
0.6 s
1.2 s
1.8 s
k·L = 3
k·L = -3
k·L = 3
k·L = -2
C
Time (s)
0
0.6
1.2
1.8
0 0.2 0.4 0.6 0.8 1
Fractional distance along centerline
(head = 0, tail = 1)
Normalized curvature (k·L)
10
5
0
−5
−10
D
Magnitude
of normalized curvature
3.0
2.5
2.0
1.5
1.0
0.5
0 0.2 0.4 0.6 0.8 1
Fractional distance along centerline
(head = 0, tail = 1)

Figure 3

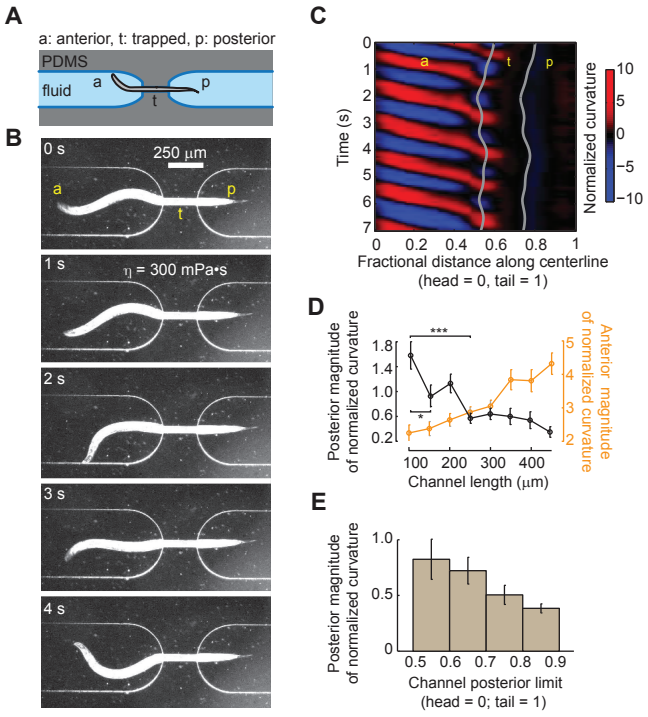
A
a: anterior, t: trapped, p: posterior
PDMS
fluid
a
t
p
B
0 s
250 μm
a
t
p
1 s
η = 300 mPa•s
2 s
3 s
4 s
C
a
t
p
Time (s)
Normalized curvature
Fractional distance along centerline
(head = 0, tail = 1)
D
Posterior magnitude of normalized curvature
Anterior magnitude of normalized curvature
Channel length (μm)
E
Posterior magnitude of normalized curvature
Channel posterior limit
(head = 0; tail = 1)

Figure 4

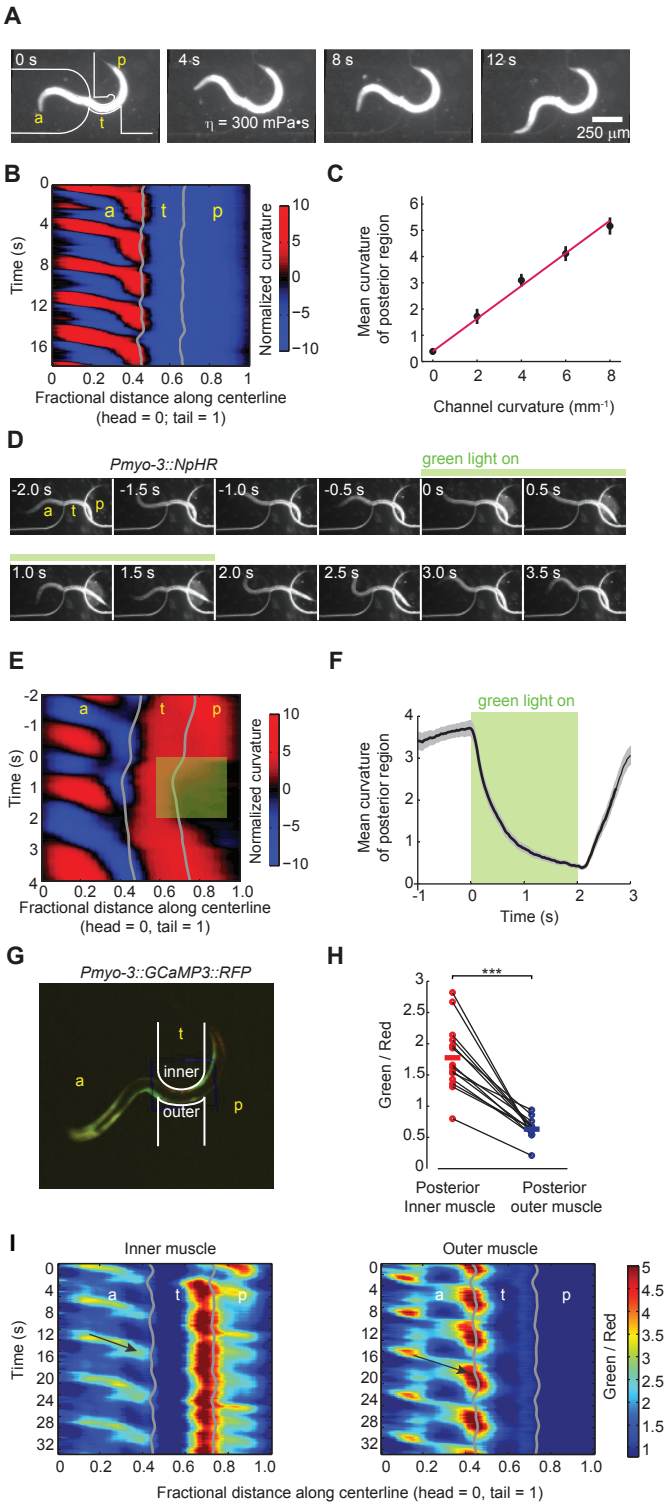
A
0 s
4 s
8 s
12 s
η = 300 mPa•s
250 μm
B
Time (s)
Normalized curvature
Fractional distance along centerline
(head = 0; tail = 1)
C
Mean curvature of posterior region
Channel curvature (mm-1)
D
Pmyo-3::NpHR
green light on
E
Time (s)
Normalized curvature
Fractional distance along centerline
(head = 0, tail = 1)
F
green light on
Mean curvature of posterior region
Time (s)
G
Pmyo-3::GCaMP3::RFP
inner
outer
H
***
Green / Red
Posterior Inner muscle
Posterior outer muscle
I
Inner muscle
Outer muscle
Time (s)
Green / Red
Fractional distance along centerline (head = 0, tail = 1)

Figure 5

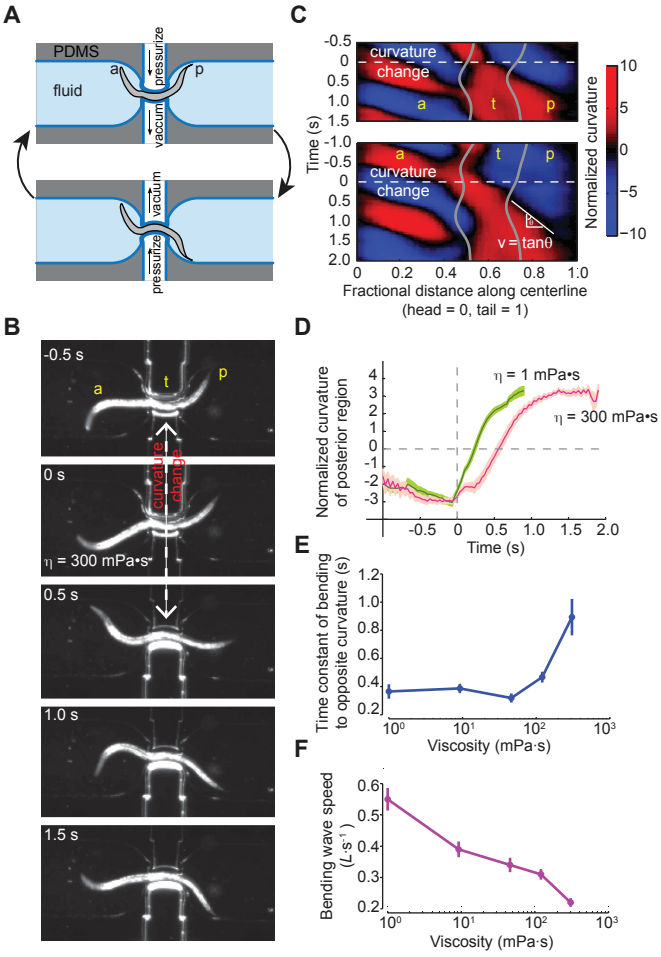
A
PDMS
fluid
a
p
pressurize
vacuum
vacuum
pressurize
B
-0.5 s
a
t
p
0 s
curvature change
η = 300 mPa•s
0.5 s
1.0 s
1.5 s
C
curvature change
a
t
p
a
t
p
curvature change
v = tanθ
Time (s)
Fractional distance along centerline
(head = 0, tail = 1)
Normalized curvature
D
η = 1 mPa•s
η = 300 mPa•s
Normalized curvature of posterior region
Time (s)
E
Time constant of bending to opposite curvature (s)
Viscosity (mPa·s)
F
Bending wave speed (L s⁻¹)
Viscosity (mPa·s)

Figure 6

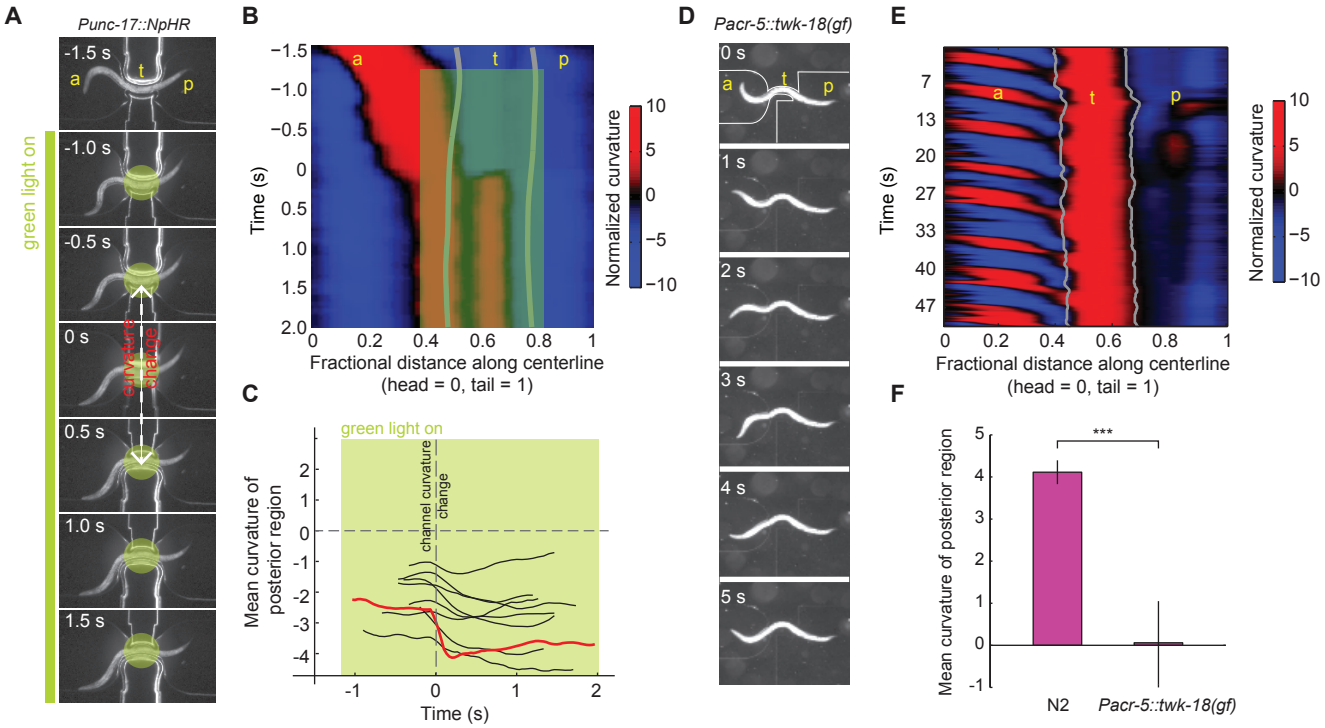
A
Punc-17::NpHR
-1.5 s
-1.0 s
-0.5 s
0 s
0.5 s
1.0 s
1.5 s
a
t
p
green light on
curvature change
B
Time (s)
Fractional distance along centerline
(head = 0, tail = 1)
Normalized curvature
C
green light on
channel curvature change
Mean curvature of posterior region
Time (s)
D
Pacr-5::twk-18(gf)
0 s
1 s
2 s
3 s
4 s
5 s
E
Time (s)
Fractional distance along centerline
(head = 0, tail = 1)
Normalized curvature
F
Mean curvature of posterior region
***
N2
Pacr-5::twk-18(gf)

Figure 7

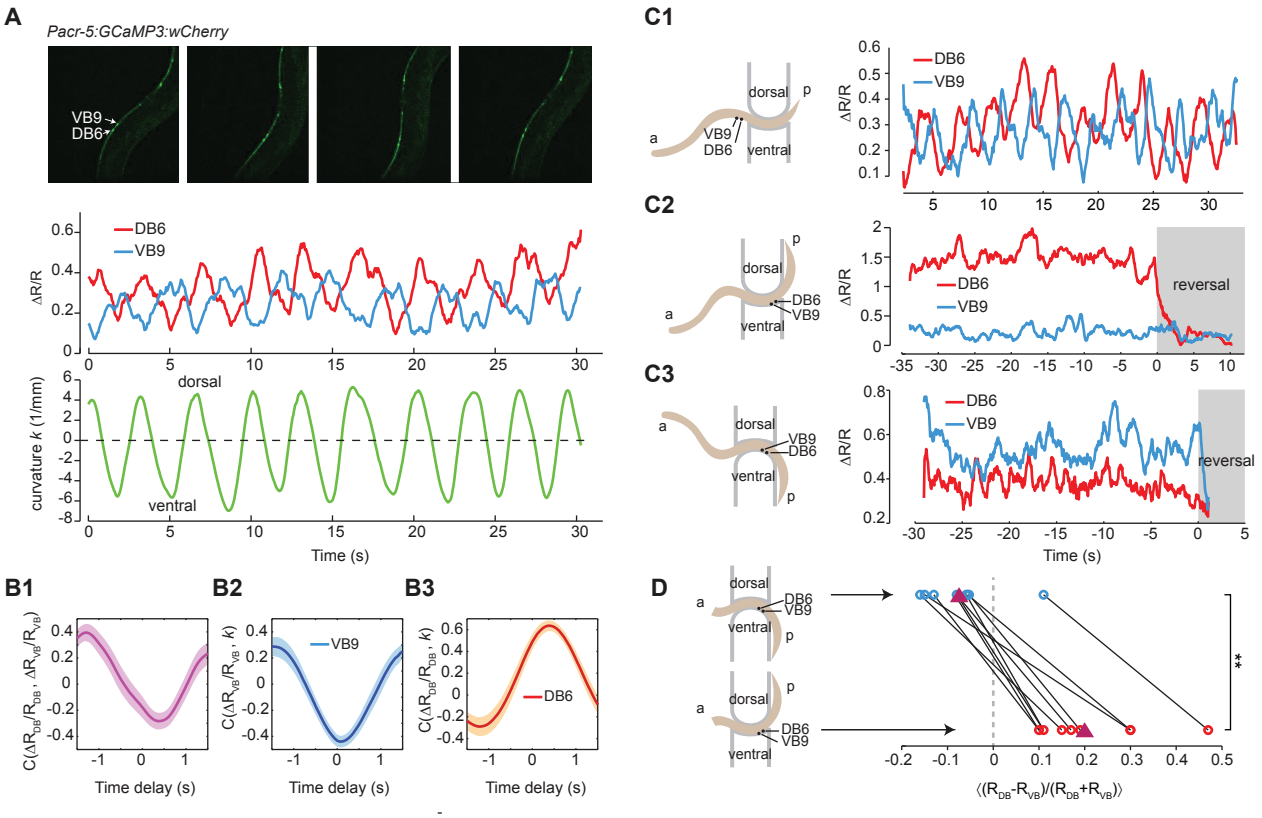
A
Pacr-5:GCaMP3:wCherry
VB9
DB6
DB6
VB9
ΔR/R
dorsal
ventral
curvature k (1/mm)
Time (s)
B1
B2
B3
VB9
DB6
Time delay (s)
C1
C2
C3
dorsal
ventral
reversal
D
⟨(R_DB-R_VB)/(R_DB+R_VB)⟩
**

Figure 8

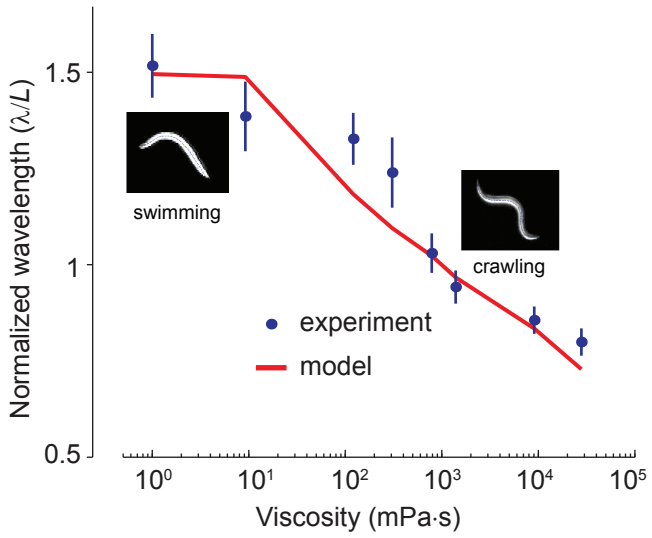
Normalized wavelength (λ/L)
1.5
1
0.5
swimming
crawling
experiment
model
10⁰
10¹
10²
10³
10⁴
10⁵
Viscosity (mPa·s)

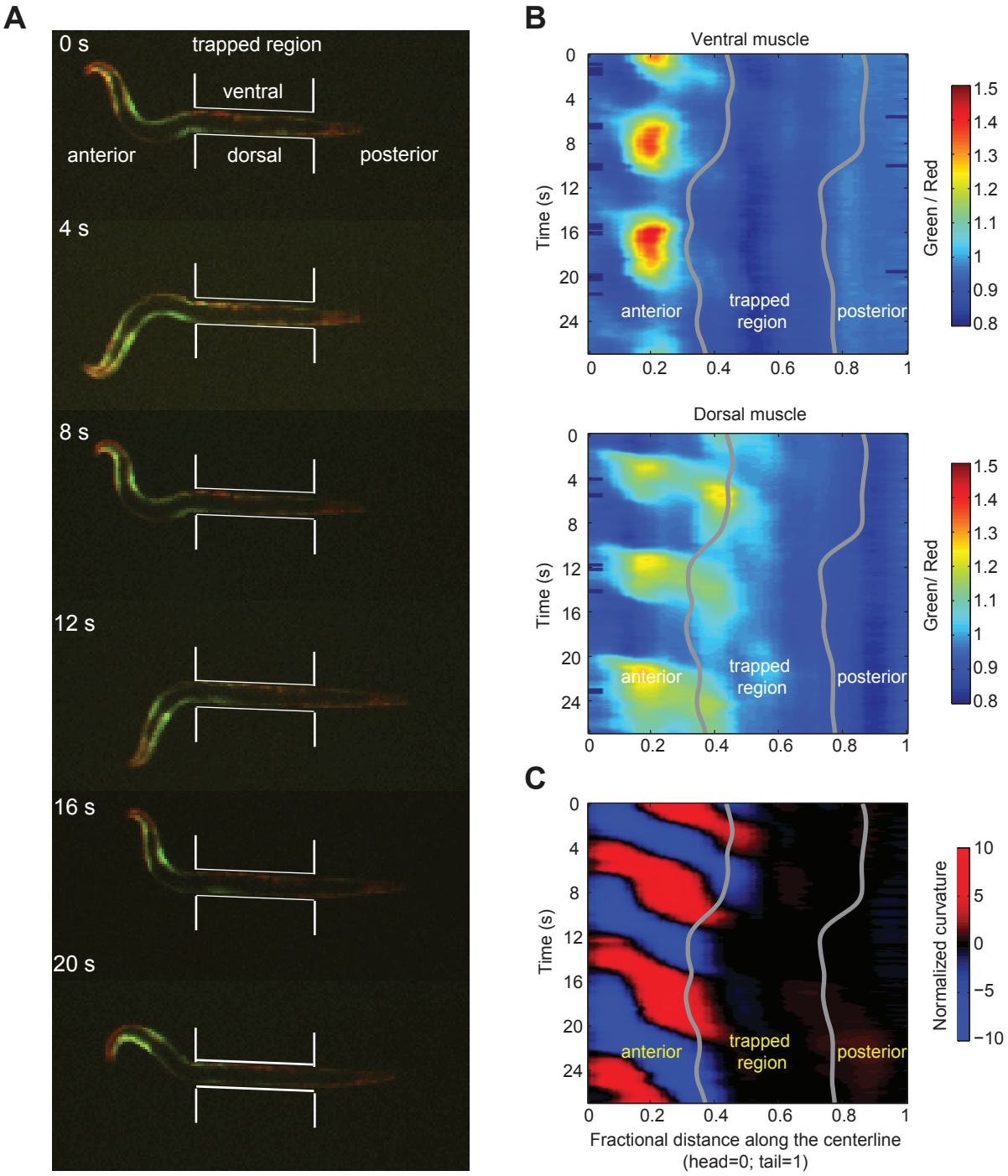

Figure S1: Intracellular calcium dynamics in muscle cells of a transgenic worm (*Pmyo3::G-CaMP3::RFP*) partially constrained in a straight microfluidic channel.

(A) Video images of a worm exhibiting forward locomotory gait while partially immobilized in a straight microfluidic channel. Red fluorescence constitutes the reference channel emanating from RFP in the muscle cells. Green fluorescence constitutes the calcium-sensitive signal emanating from G-CaMP3. White lines show the boundary of the channel (also see Supplementary Movie 2).

(B) Ratiometric analysis of intracellular calcium dynamics within the ventral and dorsal muscle cells of the worm trapped in the straight channel shown in **(A)**. Higher ratios of green to red fluorescence indicate higher intracellular calcium levels. Intracellular calcium levels in both the ventral (upper kymogram) and dorsal muscles (lower kymogram) of the posterior region emerging from the straight channel are lower than in the anterior region. Representative result from one of the five worms studied.

(C) Kymogram of time-varying body curvature for the worm trapped in the straight channel shown in **(A)** .

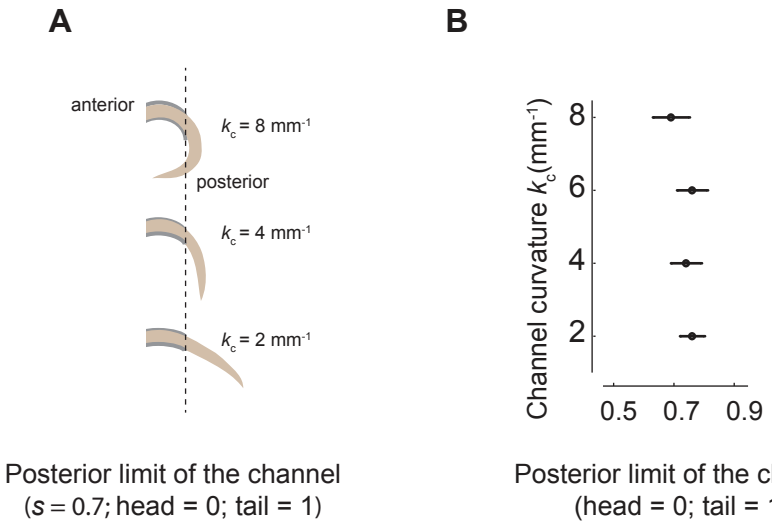

Figure S2: Position of the static curved microfluidic channel

(**A**) Schematic of a worm partially trapped in microfluidic channels with different curvatures. The position of the posterior limit of channel relative to the worm's tail is constant.
(**B**) Population measurements (mean +/- standard deviation). $n \geq 8$ worms for each condition.

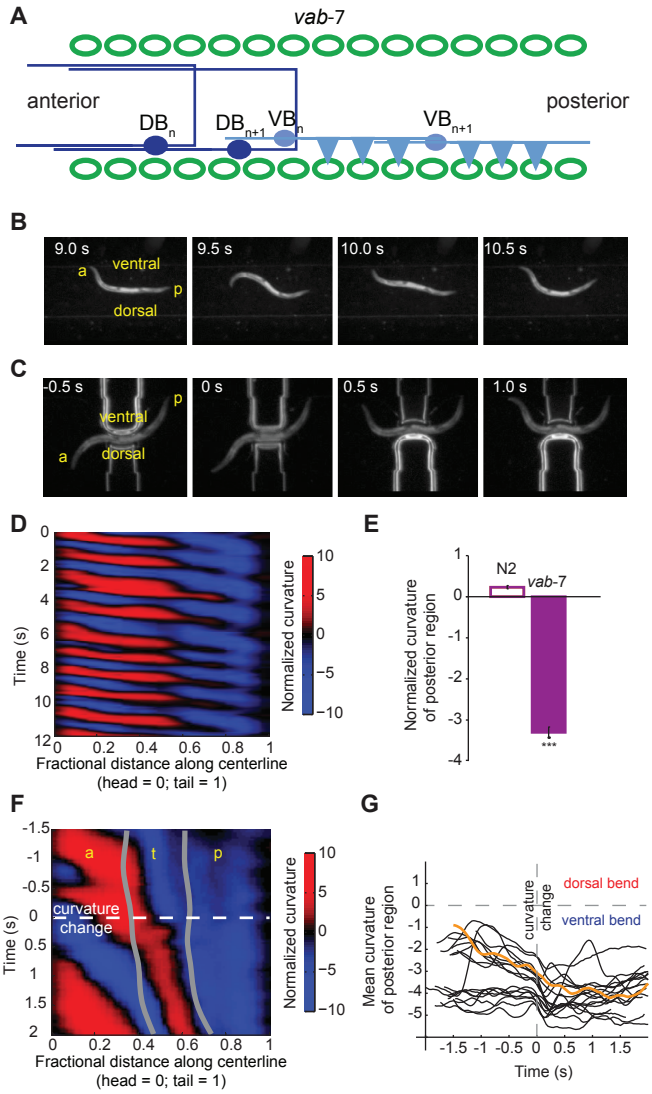

Figure S3: Undulatory wave propagation disrupted in *vab*-7 mutants.

(A) DB motor neurons switich the direction of their processes in *vab-7* mutants. (**B**,**C**) Video images of a *vab*-7 mutant worm freely swimming in water (**B**) and trapped in a pneumatic microfluidic device (**C**). Ventral and dorsal side of the worm are distinguished by using the eggs as markers.

(**D**) Kymogram of a freely swimming *vab*-7 mutant worm show bending waves propagate from head to tail. Anterior regions alternate between dorsal curvature (red) and ventral curvature (blue). Posterior regions alternate between null curvature (black) and ventral curvature (blue) (also see Supplementary Movie 9). (**E**) Curvature of the posterior body region (0.6-0.8 body length), average over an integer number of undulation periods, in a free swimming worm. n ≥ 6 for each data point. *** p < 0.001, Mann-Whitney U test.

(**F**) Kymogram of *vab*-7 mutant worm trapped in the pneumatic microfluidic device as shown in (**C**). Changing the curvature of the trapped middle region towards the dorsal side (red) does not induce dorsal curvature in the posterior region (also see Supplemental Movie 10). (**G**) Curvature of the posterior body region, measured as an average from the posterior limit of the channel to the tail, before and after the induced curvature change in the trapped middle region at t = 0. Representative trials from six worms. Orange curve corresponds to the experiment shown in (**C**) and (**F**).

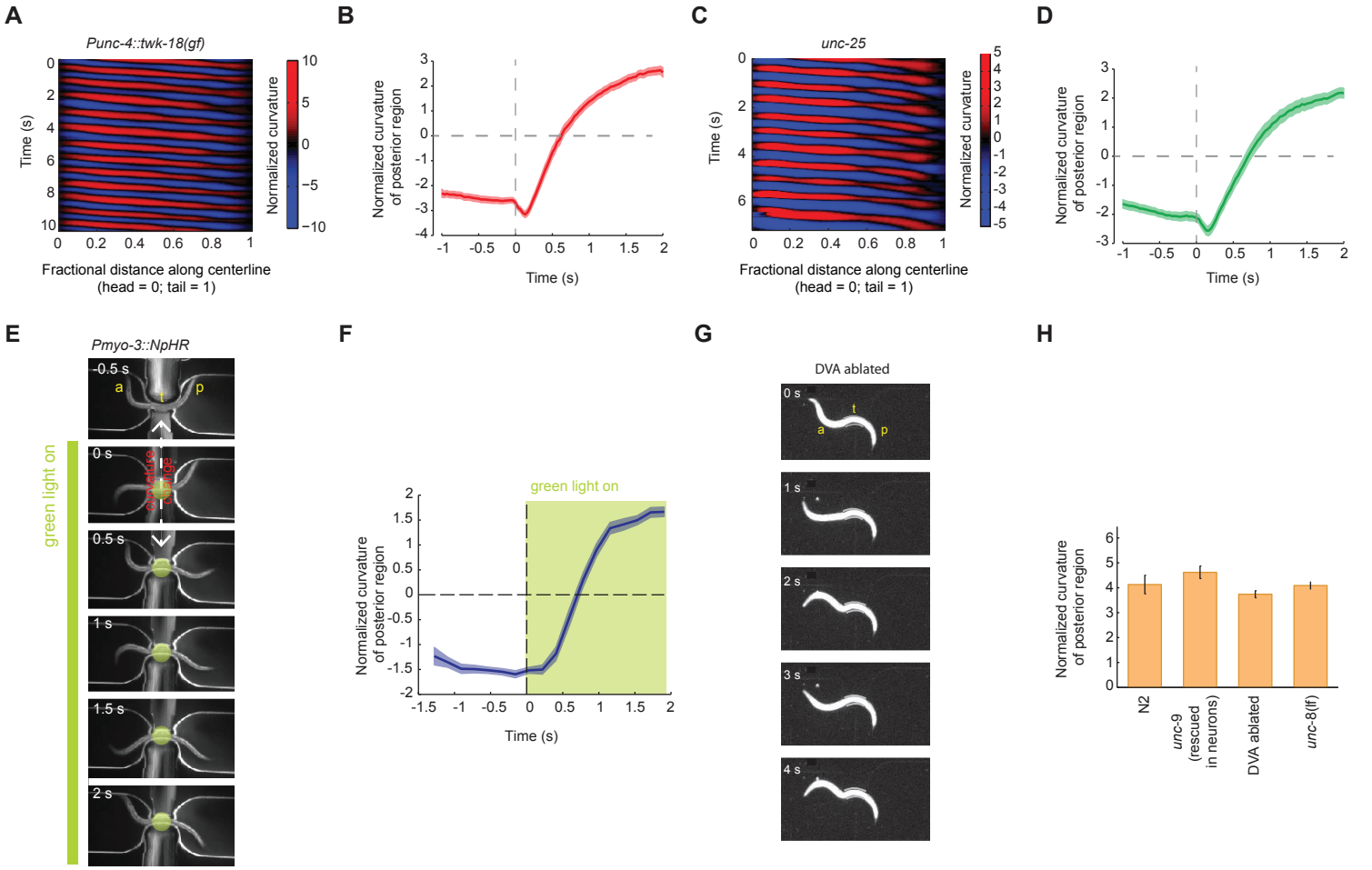

Figure S4: A-type cholinergic, D-type GABAergic motor neurons, DVA interneuron and muscles are not required for transducing the bend-sensitive signal during forward locomotion.

(A) Kymogram of a freely swimming transgenic worm (P*unc*-4::*twk*-18) in which the A-type cholinergic motor neurons are hyperpolarized due to the expression of an active K^+ channel. The bending waves during forward locomotion propagates normally from head to tail. **(B)** Curvature of the posterior body region of P*unc*-4::*twk*-18 worms trapped in the pneurmatic microfluidic device. Changing the curvature of the trapped middle region at $t = 0$ can induce a change of curvature in the posterior body region. The rising time constant is 0.814 +/- 0.072 s. 54 trials from 6 worms immersed in 300 mPa·s viscous solution. The shaded region represents s.e.m.

(C) Kymogram of a freely swimming GABA difficient *unc*-25 mutant worm shows normal bending waves propagating from head to tail. **(D)** Curvature of the posterior body region of *unc*-25 mutants trapped in the pneurmatic microfluidic device. Changing the curvature of the trapped middle region at $t = 0$ can induce a change of curvature in the posterior body region emerged from the channel. The rising time constant is 1.02 +/- 0.16 s. 38 trials from 7 worms immersed in 300 mPa·s viscous solution. The shaded region represents s.e.m.

(E) Representative video images of a transgenic worm (P*myo*-3::NPHR) trapped in the pneumatic microfluidic device. The worm expresses Halorhodopsin in all muslce cells. Green light induced hyperpolarization of the body wall muscles trapped within the inflatable channel does not affect the proprioceptive coupling. Changing the curvature of the trapped middle region at $t = 0$ can still induce a change of curvature in the posterior body region. **(F)** Population data from 7 worms immersed in 300 mPa·s viscous solution. The rising time constant is 1.2 +/- 0.2 s.The shaded region represents s.e.m.

(G) Representative video images of a DVA ablated worm partially trapped in the static microfluidic channel. Again, the posterior body region emerged from the channel is compelled to bend in the same direction as the channel, suggesting that DVA interneuron is not involved in the observed proprioceptive coupling. **(H)** Same experiments were also carried out on *unc*-8(lf) mutants and *unc*-9 mutants in which the UNC-9 innexin protein was rescued in all neurons. UNC-8 encodes a mechanically gated ion channel that is thought to be involved in proprioception by acting on the motor neurons. The *unc*-9 rescued strain would have gap junction deficiency only in muscles. However, neither this putative channel nor gap junction coupling between muscles is required to transduce the observed proprioceptive coupling. The posterior body region emerged from the channel exhibits static curvature that is not significantly different from the wild type N2. One-Way ANOVA, $p > 0.05$, $n \geq 6$ worms for each case.

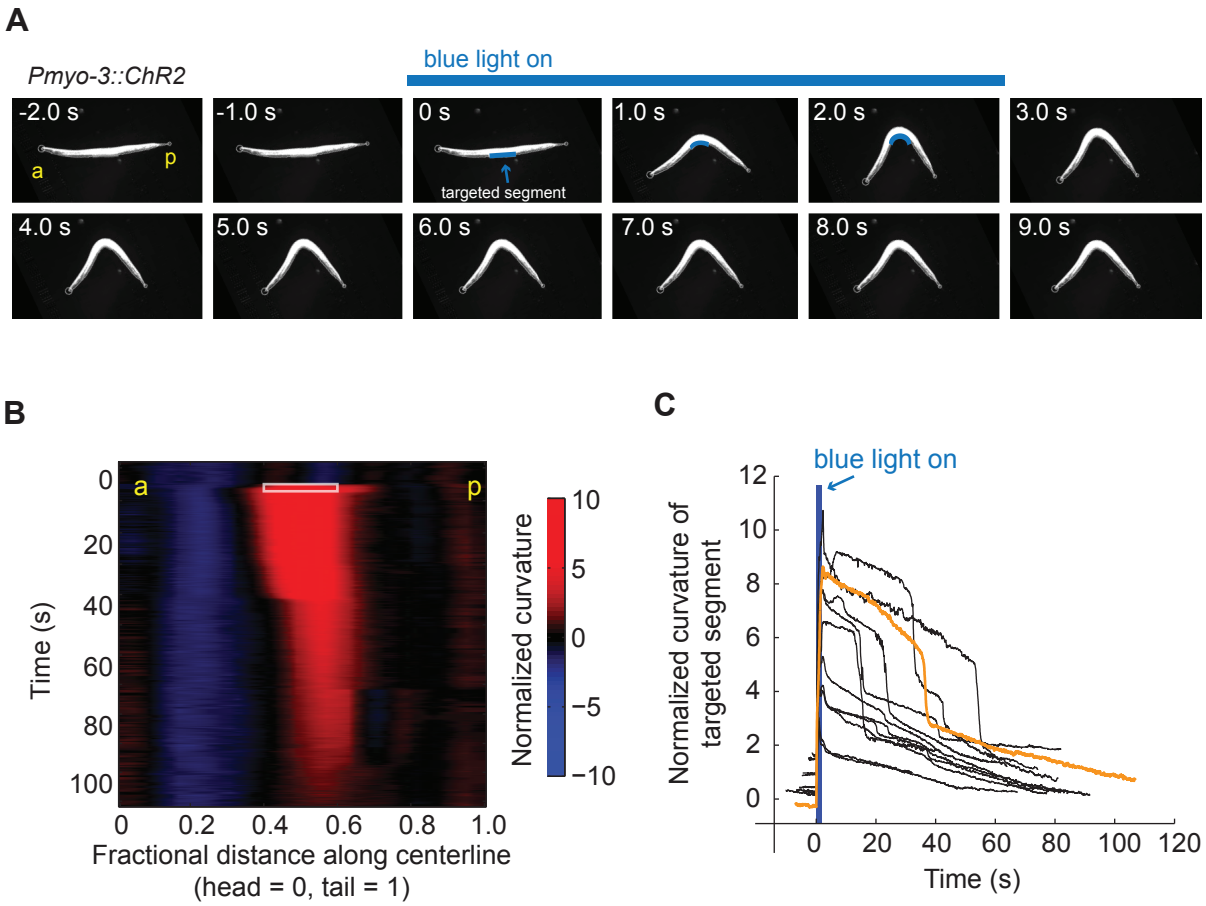

Figure S5: Muscle hysteresis induced by optogenetic illumination.

(A) Video images of an ivermectin-treated transgenic worm (P*myo*-3::ChR2). In a 2 s interval, a targeted rectangular region near the middle of the worm (blue rectangle superposed on video images) was illuminated by blue light to induce body bending (also see Movie S10).

(B) Curvature kymogram of the animal shown in **(A)**. White rectangle marks the region and duration of blue light illumination.

(C) Normalized curvature of the targeted region before and after illumination. Data from three different worms are shown. Orange data points correspond to the experiment shown in **(A)** and **(B)**.

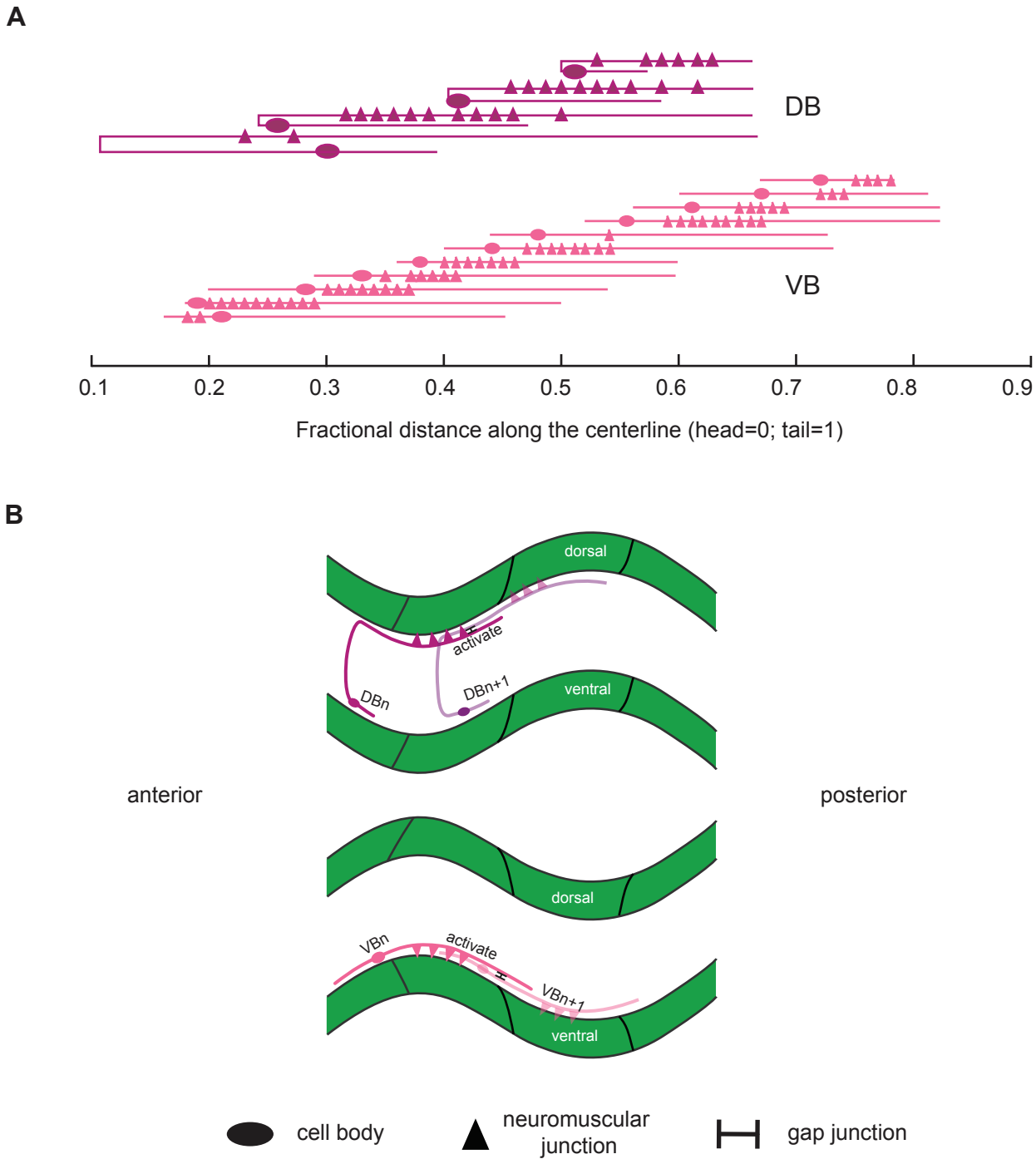

Figure S6: anatomy of B-type motor neurons supports proprioceptive coupling from anterior to posterior body regions.

(A) Actual spatial layouts of motor neurons. Cell bodies are denoted by circles and neuromuscular junctions by triangles. Note that not all the B-type motor neurons and their connections have been fully reconstructed (modified from Chen, B.L., PhD thesis CSHL, 2007). **(B)** To transduce the proprioceptive signal from anterior to posterior body region, we postulate that the processes in the *anterior* portion of VB/DB motor neurons are bend-sensitive. As the neuromuscular junctions of a motor neuron highly overlap with the anterior processes of the neighboring motor neuron of the same class, Bending of one segment can activate the adjacent posterior VB/DB motor neuron. The gap junctions that couple the motor neurons of the same class may also facilitate the transduction of the proprioceptive signals.

Supplementary Experimenal Procedures

Strains and constructs The *vab-7* mutant strain and MP145 *unc-8(e15lb145)* were obtained from the *C. elegans* Genetics Center (Minneapolis, MN, USA). The *unc-13*(*s69*) mutant strain was a gift from E. Jorgensen (University of Utah).

For calcium imaging experiments in body wall muscles, transgenic worms AQ2953 *ljIs131* (P*myo-3*::*GCaMP3-UrSL-RFP*) were used. The promoter sequence of the *Pmyo-3* gene (Kuroyanagi et al., 2006) and the coding sequences of GCaMP3 and tagRFP-T were ligated to the pSM backbone. The *GCaMP3* and tagRFP-T sequences were separated by a SL2 trans-splicing site. The construct was injected into N2 worms to obtain extrachromosomal arrays. For B motor neuron imaging, an integrated transgenic line ZM6600 *hpIs264* (pJH2524, P*acr-5*::*GCaMP3-UrSL-wCherry*) were used. wCherry is mCherry optimized for expression in *C. elegans* (a gift from A. Desai, University of California, San Diego, CA, USA).

For motor neuron silencing experiments, ZM5097 *lin-15; hpEx2073 (*pJH2107 P*acr5::twk-18(gf)-UrSL-wCherry)* and ZM5259 *lin-15; hpEx2171* (pJH2108 P*unc-4::twk-18(gf)-UrSL-wCherry)* were used. For testing the contribution of UNC-9 gap junctions in muscle, ZM2509 *hpIs3 unc-9(fc16); hpEx803 (*pJH1001 P*rgef-1-unc-9cDNA) + odr-1)* was used. For DVA ablation, KP6828 (*Pnlp-12::GFP*) strain was used (a gift from J. Kaplan, Massachusetts General Hospital).

The transgenic worms used in all optogenetic experiments were cultivated in the dark at 20^{o}C on NGM plates with *Escherichia coli* OP50 and all-*trans* retinal. We made OP50-retinal plates by seeding each 6-cm NGM plate with 250 µl OP50 and 1 µl 100 mM retinal in ethanol. Strains used are ZX444 [*lin-15*(n765ts); *zxEx29* (P*myo-3::NpHR::ECFP*; *lin-15*+)] (a gift from A. Gottschalk), ZM5016 *hpls178*[P*unc-17::NpHR::ECFP*] and ZM5398 *hpls199*[pJH2086 P*myo-3::ChR2::EGFP]*. All *hpIs* lines were integrated using a UV crosslinker, and the resulting integrants were outcrossed at least 4 times against the N2 wild-type strain. The strain *unc-*

13(s69); *hpls199*[P*myo-3::ChR2::EGFP*] was made by crossing *unc-13(s69)* with ZM5398 *hpls199.*

Microfluidic devices Microfluidic devices were fabricated using standard soft lithography. Each design was drawn in Clewin and sent to a laser-printing service (CAD/Art Services, Inc. Bandon, OR). A master was created by patterning features of SU-8 negative photoresist (Microchem Corp., Newton, MA, USA) on a silicon wafer using photolithography. This master was then used to mold microfluidic channels in PDMS. To facilitate the release of the PDMS device from the master, we treated the master with vapor of tridecafluoro (1,1,2,2 tetrahydroooctyl) trichlorosilane (Gelest, Inc., Philadelphia, PA, USA) inside a vacuum chamber. The PDMS prepolymer was mixed with Sylgard 184, its curing agent, at specific weight ratios (20:1 for the pneumatic microfluidic device and 10:1 for other devices). After pouring the PDMS prepolymer over the master, we cured the PDMS at 60°C for 8 h and peeled the PDMS slab from the master. A circular biopsy punch (1.5 mm in diameter, Shoney Scientific Inc., Waukesha, WI) was used to create inlets and outlets for the microfluidic channels. The PDMS slab was bonded to a glass coverslip by treating the surfaces of the glass and the PDMS slab with air plasma for two minutes and 30 seconds respectively. The PDMS was bonded to another PDMS slab in the pneumatic microfludic device.

Measuring locomotion of partially immobilized worms Experiments were performed on Nikon microscopes (TE2000 or Eclipse LV150) under 4X magnification with dark field illumination. Image sequences were taken by a CCD camera (Imaging Source) and recorded on a computer at 30 Hz using IC Capture software (Imaging Source).

Image analysis was performed using custom software written in MATLAB (MathWorks, Inc. Natick, MA) following methods described in (Fang-Yen et al., 2010). Briefly, we identified image sequences in which the worm persistently exhibited its forward undulatory gait, i.e., bending waves propagated backward from the head. After background subtraction to eliminate features of the microfluidic channel, we filtered and thresholded each image to obtain a binary image. The head and tail were identified as the points of maximum convex curvature on the worm boundary. A centerline extending from the head to the tail of the worm was calculated so

that each point is roughly equidistant to nearest boundary points on two sides of the animal. The centerline was then fit by a least-squares cubic smoothing spine. Curvature, by definition, was calculated as the magnitude of the derivative of the unit vector tangent to the centerline with respect to the body coordinate along the centerline.

Ivermectin-induced paralysis Young adult transgenic worms (*hpls199* pJH2086[P*myo-3::ChR2::EGFP*] or *unc-13*; *hpls199*) were placed in ivermectin solution (0.02 mg/mL in NGM) sandwiched between two glass sides separated by 127 μm. Worms were free to swim until completely paralyzed after ~30 min, when they were used for optogenetic stimulation.

Laser ablation Laser ablation was conducted using the MicroPoint ablation system (Andor). DVA neuron was ablated in animals at L3 larvae stage. Behavioral experiments were performed in adults when the green fluorescence marker that labels DVA soma and axon completely disappeared.

A minimum model for coordinating forward movement in *C. elegans* We model the worm locomotory circuit as a set of 5 discrete units labeled by $i \in [1,5]$. Although the *C. elegans* wiring diagram does not suggest discrete segments, our division of the worm motor circuit into five segments reflects the division of total worm length L (~ 1 mm) by the spatial extent of proprioceptive coupling (~ 200 μm inferred from Figure 3D). Muscle activity in one segment receives positive stretch-sensitive feedback from its nearest anterior neighbor, which can be mathematically stated in the simplest model for linear coupling:

$$\tau_c \frac{dX_i}{dt} = -X_i + c\kappa_{i-1}; \; i \geq 2 \tag{1}$$

In this equation, the sign and magnitude of X_i characterizes the direction and strength of muscle activity in each segment of worm length (i.e., $X_i > 0$ indicates higher dorsal muscle activity, $X_i < 0$ reflects higher ventral muscle activity). Coupling of the curvature of an anterior segment (κ_{i-1}) to the activity of the nearest neighboring ith segment (X_i) is positive and proportional to the coupling constant ($c > 0$). To begin, we assume that muscle activity decays exponentially with τ_c

as the decay time constant. This formulation allows us to calculate the dynamics of the system analytically.

Next, we relate muscle activity to the time-varying shape of the worm. Because of the mechanical drag imposed by the environment, the shape of a body segment does not instantaneously follow the muscle torque. Following our previous work(Fang-Yen et al., 2010), the relation between shape and torque can be derived by solving the dynamics of an elastic rod bent in viscous medium at low Reynolds number, which leads to

$$C_N \frac{\partial \kappa}{\partial t} + b \frac{\partial^4 \kappa}{\partial s^4} = \frac{\partial^4 M}{\partial s^4}, \tag{2}$$

where C_N is the frictional drag coefficient normal to the body centerline, b is the bending modulus of the worm body, M is the active muscle torque and s is the spatial coordinate along the centerline of the worm. This relation is further simplified for a sinusoidal wave of muscular activities $M = M_0 e^{i(2\pi s/\lambda - \omega t)}$, where M_0 is the magnitude of the active muscle torque. For self-consistency, we assume that this is indeed the case since our model is by construction to generate approximately sinusoidal bending waves. As a result, we found that

$$\kappa_i + \tau_\eta \frac{d\kappa_i}{dt} = M / b, \tag{3}$$

where

$$\tau_\eta = \frac{C_N}{b} (\lambda / 2\pi)^4. \tag{4}$$

In Eq. (4), λ is the wavelength of undulation, τ_η reflects the time scale during which a passive (e.g., anesthetized) nematode relaxes to a flat shape after being bent. It is proportional to the viscosity of the medium. The relation between active torque M and the relative muscle activity X is given by $M = M_0 X$. Then we may rewrite Eq. (3) as

$$\kappa_i + \tau_\eta \frac{\partial \kappa_i}{\partial t} = M_0 X_i / b. \tag{5}$$

To derive the wavelength of body undulation, let us first calculate the phase difference between the curvatures of two adjacent segments. Given $\kappa_{i-1} = |\kappa_{i-1}| e^{-i\omega t}$, by solving Eqs. (1) and (5), we have

$$\kappa_i = \frac{|\kappa_{i-1}| cM_0 / b}{\sqrt{(1+\omega^2\tau_c^2)(1+\omega^2\tau_\eta{}^2)}} e^{-i\omega t+\varphi}, \tag{6}$$

where the phase difference

$$\varphi = \arctan(\omega\tau_c) + \arctan(\omega\tau_\eta). \tag{7}$$

To the first order approximation, we have

$$\varphi \approx \omega(\tau_c + \tau_\eta). \tag{8}$$

The expression for the wavelength of undulation is given by

$$\lambda = 2\pi l / \varphi, \tag{9}$$

where l is the segment length. By substituting Eq. (9) into Eq. (8), we arrived at Eq. (1) in the main text.

In this simple model, time delays from proprioceptive coupling and external mechanical drag imposed by the environment contribute to the phase lag of curvature between adjacent segments. In a more sophisticated model, one might want to incorporate other contributions. For example, because muscle is power limited, muscle contraction is also speed limited. Nevertheless, the intrinsic delays within the muscles and other processes within the neuromuscular network could all be represented by a single parameter τ_c in Eq. (8).

Supplementary References

Fang-Yen, C., Wyart, M., Xie, J., Kawai, R., Kodger, T., Chen, S., Wen, Q., and Samuel, A.D. (2010). Biomechanical analysis of gait adaptation in the nematode Caenorhabditis elegans. Proc Natl Acad Sci U S A 107, 20323-20328.

Kuroyanagi, H., Kobayashi, T., Mitani, S., and Hagiwara, M. (2006). Transgenic alternative-splicing reporters reveal tissue-specific expression profiles and regulation mechanisms in vivo. Nat Methods 3, 909-915.

Supplementary Movie Legends

Movie S1

A young adult N2 worm was swimming forward in dextran solution [20% dextran in NGM (wt/vol)] while the middle region of its body was constrained in a straight microfluidic channel. Body undulation can propagate to the anterior limit of the channel, but bending waves emerging from the posterior limit of the channel were hardly detected and the unrestricted posterior body region remained straight.

Movie S2

A young adult transgenic worm expressing calcium indicators in body wall muscle cells (P*myo-3*::*GCaMP3*::*RFP*) was swimming forward in dextran solution [15% dextran in NGM] while the middle region of its body was constrained in a straight microfluidic channel. White lines show the boundary of the channel. Pseudo-color shows the ratio of green fluorescence (emitted from GCaMP3) to red fluorescence (from RFP). Higher ratio, which indicates higher calcium activities, is represented by a larger value of the red component in the muscle color map. Muscle cells within and posterior to the channel had lower levels of intracellular calcium dynamics than muscle cells anterior to the channel that drove bending waves.

Movie S3

A young adult N2 worm was swimming forward in dextran solution (20% dextran in NGM) while the middle region of its body was constrained in a curved microfluidic channel. The unrestricted posterior region of the worm that exhibited static curvature in the same direction as that imposed on the middle region by the channel.

Movie S4

A young adult transgenic worm that expresses halorhodopsin in body wall muscles (P*myo-3*::*NpHR*) was swimming forward in dextran solution (20% dextran in NGM) while the middle region of its body was constrained in a curved microfluidic channel. A bright circular spot appeared when the posterior body region was illuminated by green light. During illumination, the unstrained posterior body region was reversibly straightened.

Movie S5

A young adult transgenic worm that expresses calcium indicators in body wall muscle cells (P*myo-3*::*GCaMP3*::*RFP*) was swimming forward in dextran solution (15% dextran in NGM) while the middle region of its body was constrained in a curved microfluidic channel. White lines show the boundary of the channel. Pseudo-color shows the ratio of green fluorescence (from *GCaMP3*) to red fluorescence (from *RFP*). Higher ratio is represented by a larger value of the red component in the muscle color map. During forward locomotion, the muscle cells at the inner side of the posterior body region emerging from the channel consistently exhibited higher calcium activities than the outer side.

Movie S6

After fully paralyzed by sodium azide, a young adult N2 worm was partially constrained in a curved pneumatic microfluidic channel. The unrestrained body regions emerged from the channel always remained straight.

Movie S7

Young adult N2 worms were moving forward while the middle regions of their bodies are constrained in pneumatic microfluidic channels. In the first half of the movie, a worm was swimming forward in NGM buffer solution. Switching the bending direction of the channel quickly induces the switch in the bending direction of the posterior body region. In the second half of the movie, a worm was swimming forward in more viscous fluid (20% dextran solution in

NGM). In this case, there is a more significant delay between switching the bending of the channel and switching the bending direction in the posterior body region.

Movie S8

A young adult transgenic worm (P*unc-17*::*NpHR*) that expressed halorhodopsin in all cholinergic motor neurons was moving forward while the middle region of the body was constrained in an pneumatic microfluidic channel. During green light illumination, the unrestrained posterior body region failed to follow the switch of channel curvature.

Movie S9

A young adult transgenic worm [*Pacr-5::twk-18(gf)*] in which B-type motor neurons were inactivated due to the expression of an active K^+ channel. The worm strived to move forward while the middle region of its body was constrained in a curved microfluidic channel. The posterior body region emerged from the channel no longer follows the curvature of the channel.

Movie S10

This movie shows two-second blue light illumination of an ivermectin-treated paralyzed transgenic worm (P*myo-3*::*ChR2*). When DLP was on, blue light illuminated a rectangular region near the middle of the worm and induced body bending. When DLP was off, there was no light stimulation but the bending persisted for a long period.

Supplemental Movie 1

Click here to download Supplemental Movies and Spreadsheets: Supplementary_movie1.mov

Supplemental Movie 2

Click here to download Supplemental Movies and Spreadsheets: Supplementary_movie2.mov

Supplemental Movie 3

Click here to download Supplemental Movies and Spreadsheets: Supplementary_Movie3.mov

Supplemental Movie 4

Click here to download Supplemental Movies and Spreadsheets: Supplementary_movie4.mov

Supplemental Movie 5

Click here to download Supplemental Movies and Spreadsheets: Supplementary_movie5.mov

Supplemental Movie 6

Click here to download Supplemental Movies and Spreadsheets: Supplementary_movie6.mov

Supplemental Movie 6

Click here to download Supplemental Movies and Spreadsheets: Supplementary_movie7.mov

Supplemental Movie 8

Click here to download Supplemental Movies and Spreadsheets: Supplementary_movie8.mov

Supplemental Movie 9

Click here to download Supplemental Movies and Spreadsheets: Supplementary_movie9.mov

Supplemental Movie 10

Click here to download Supplemental Movies and Spreadsheets: Supplementary_movie10.mov